

## A toolbox for generating scalable mitral valve morphometric models

de Oliveira, Diana C.; Espino, Daniel M.; Deorsola, Luca; Mynard, Jonathan P.; Rajagopal, Vijay; Buchan, Keith; Dawson, Dana; Shepherd, Duncan E. T.

DOI:

[10.1016/j.combiomed.2021.104628](https://doi.org/10.1016/j.combiomed.2021.104628)

License:

Creative Commons: Attribution-NonCommercial-NoDerivs (CC BY-NC-ND)

*Document Version*

Peer reviewed version

*Citation for published version (Harvard):*

de Oliveira, DC, Espino, DM, Deorsola, L, Mynard, JP, Rajagopal, V, Buchan, K, Dawson, D & Shepherd, DET 2021, 'A toolbox for generating scalable mitral valve morphometric models', *Computers in Biology and Medicine*, vol. 135, 104628. <https://doi.org/10.1016/j.combiomed.2021.104628>

[Link to publication on Research at Birmingham portal](#)

### General rights

Unless a licence is specified above, all rights (including copyright and moral rights) in this document are retained by the authors and/or the copyright holders. The express permission of the copyright holder must be obtained for any use of this material other than for purposes permitted by law.

- Users may freely distribute the URL that is used to identify this publication.
- Users may download and/or print one copy of the publication from the University of Birmingham research portal for the purpose of private study or non-commercial research.
- User may use extracts from the document in line with the concept of 'fair dealing' under the Copyright, Designs and Patents Act 1988 (?)
- Users may not further distribute the material nor use it for the purposes of commercial gain.

Where a licence is displayed above, please note the terms and conditions of the licence govern your use of this document.

When citing, please reference the published version.

### Take down policy

While the University of Birmingham exercises care and attention in making items available there are rare occasions when an item has been uploaded in error or has been deemed to be commercially or otherwise sensitive.

If you believe that this is the case for this document, please contact [UBIRA@lists.bham.ac.uk](mailto:UBIRA@lists.bham.ac.uk) providing details and we will remove access to the work immediately and investigate.

# 1 **A toolbox for generating scalable mitral valve morphometric models**

2  
3 Diana C. de Oliveira<sup>a,\*</sup>, Daniel M. Espino<sup>a</sup>, Luca Deorsola<sup>b</sup>, Jonathan P. Mynard<sup>c,d,e,f</sup>, Vijay  
4 Rajagopal<sup>c</sup>, Keith Buchan<sup>g</sup>, Dana Dawson<sup>h,i</sup>, Duncan E.T. Shepherd<sup>a</sup>

5  
6 <sup>a</sup> Department of Mechanical Engineering, University of Birmingham, Edgbaston,  
7 Birmingham, B15 2TT

8 \* Corresponding author: DMC795@student.bham.ac.uk

9  
10 <sup>b</sup> Paediatric Cardiac Surgery, Ospedale Infantile Regina Margherita Sant Anna, Turin, 10126,  
11 Italy

12  
13 <sup>c</sup> Department of Biomedical Engineering, The University of Melbourne, Melbourne, VIC  
14 3010, Australia

15  
16 <sup>d</sup> Heart Research, Murdoch Children's Research Institute, Royal Children's Hospital,  
17 Melbourne, VIC 3052, Australia

18  
19 <sup>e</sup> Department of Paediatrics, The University of Melbourne, Melbourne, VIC 3010, Australia

20  
21 <sup>f</sup> Department of Cardiology, Royal Children's Hospital, Melbourne, VIC 3052, Australia

22  
23 <sup>g</sup> Department of Cardiothoracic Surgery, Aberdeen Royal Infirmary, Aberdeen, AB24 2ZN,  
24 Scotland

25  
26 <sup>h</sup> School of Medicine, University of Aberdeen, Aberdeen, AB25 2ZD, Scotland

27  
28 <sup>i</sup> Cardiology Department, Aberdeen Royal Infirmary, Aberdeen, AB25 2ZN, Scotland

42 **Abstract**

43 The mitral valve is a complex anatomical structure, whose shape is key to several traits of its  
44 function and disease, being crucial for the success of surgical repair and implantation of  
45 medical devices. The aim of this study was to develop a parametric, scalable, and clinically  
46 useful model of the mitral valve, enabling the biomechanical evaluation of mitral repair  
47 techniques through finite element simulations.

48 MATLAB was used to parameterize the valve: the annular boundary was sampled from a  
49 porcine mitral valve mesh model and landmark points and relevant boundaries were selected  
50 for the parameterization of leaflets using polynomial fitting. Several geometric parameters  
51 describing the annulus, leaflet shape and papillary muscle position were implemented and  
52 used to scale the model according to patient dimensions. The developed model, available as a  
53 toolbox, allows for the generation of a population of models using patient-specific  
54 dimensions obtained from medical imaging or averaged dimensions evaluated from empirical  
55 equations based on the Golden Proportion.

56 The average model developed using this framework accurately represents mitral valve  
57 shapes, associated with relative errors reaching less than 10% for annular and leaflet length  
58 dimensions, and less than 24% in comparison with clinical data. Moreover, model generation  
59 takes less than 5 minutes of computing time, and the toolbox can account for individual  
60 morphological variations and be employed to evaluate mitral valve biomechanics; following  
61 further development and validation, it will aid clinicians when choosing the best patient-  
62 specific clinical intervention and improve the design process of new medical devices.

63

64 **Keywords:** anatomy, biomechanics, computational, mitral valve, morphometry, parametric  
65 model

66

67

68

69

70

71

72

## 73 1. Introduction

74 The mitral valve (MV) is an anatomical structure, whose physiological function relies  
75 on the biomechanical properties and structural integrity of its components (Al-Atabi et al.,  
76 2012, Espino et al., 2007). Its shape is key to several traits of its function and disease, as  
77 shown by clinical (Lee et al., 2013, Sun et al., 2019), *in silico* (Pham et al., 2017, Caballero et  
78 al., 2020) and *in vitro* (Espino et al., 2007) studies. MV shape alterations, such as annular  
79 dilation or papillary muscle (PM) displacement, can affect MV performance, leading to  
80 regurgitation and resulting in suboptimal ventricular filling or ejection (Kohli et al., 2021,  
81 Cong et al., 2018).

82 Some common surgical interventions of the mitral valve include annuloplasty, leaflet  
83 resection, edge-to-edge repair or chordal replacement/transposition. Altering MV geometry  
84 during repair leads to changes in blood flow patterns, valve closure and ultimately disrupts  
85 normal flow through the left ventricle (LV) (Xu et al., 2021). Moreover, high/abnormal  
86 stresses which are induced on the valve leaflets post-repair may lead to post-surgical failure  
87 or impairment of valvular function (Kong et al., 2020). Therefore, the success of MV repair  
88 depends on the restoration of normal fluid dynamics, usually involving correction of valve  
89 mechanics (Al-Atabi et al., 2012). MV geometry has been exploited to improve the design of  
90 medical devices through the development of annuloplasty ring designs which 1) mimic the  
91 native annular saddle-shape (Doll et al., 2019) and 2) optimise load bearing by the annulus  
92 (Ncho et al., 2020), for example. The evaluation of pre- and post-operative scenarios which  
93 account for a subject's MV shape have the potential to improve surgical planning,  
94 specifically patient-specific repair procedures (Kohli et al., 2021, Walczak et al., 2021).

95 Computational studies have focused on diseased MV shapes (Caballero et al., 2019,  
96 Biffi et al., 2019, Aguilera et al., 2021) and surgical procedures (Choi et al., 2020, Caballero  
97 et al., 2020, Kong et al., 2018), either using structure-only finite element (FE) analysis (which  
98 allows to study leaflet stress patterns), or fluid-structure interaction (FSI) simulations (which  
99 accounts for the interaction between blood flow and the structure of the valve). The accuracy  
100 of these models is sensitive to valve geometry; however, even though several MV models  
101 from the literature are based on patient-specific geometries obtained from medical imaging,  
102 the associated generation process can be time consuming and computationally expensive,  
103 especially when employing numerical mesh-based approaches (Zhang et al., 2019).  
104 Moreover, deductions made from a patient-specific case cannot be generalized, since multiple  
105 patient-specific models are required for statistical power (Biau et al., 2008).

106 To overcome these limitations, parametric models, whose geometrical features are  
107 described by constraints such as specific dimensions/measurements, can be used. Some  
108 parametric MV models lack the anatomical detail that is necessary to be of clinical value,  
109 including only a simplistic representation of the leaflets (Salgo et al., 2002, Shen et al., 2017,  
110 Domenichini and Pedrizzetti, 2015). Other studies have included more complete parametric  
111 geometries including chordae tendineae and PM tips (Choi et al., 2016, Alleau et al., 2019),  
112 while more advanced parameterization frameworks have been recently developed to generate  
113 patient-specific MV surface models from measurements obtained via medical imaging  
114 (Lichtenberg et al., 2020, Pasta et al., 2020). While these advanced frameworks can generate  
115 high quality MV models within a reasonable time frame, they can only be applied to each  
116 specific patient individually, not offering the flexibility required to allow for the evaluation of  
117 how specific dimensions of MV geometry affects its function, for example.

118 Multiple *in vivo* (Warraich et al., 2012, Deorsola and Bellone, 2018, Oliveira et al.,  
119 2020) and *ex vivo* (Duplessis and Marchand, 1964, Okamoto et al., 2007) morphometric  
120 studies have attempted to correlate different dimensions of the MV geometry. Nonetheless, a  
121 unifying mathematical model that can be employed to generate an average MV geometry has  
122 been lacking in the literature. Given the importance of MV shape on the long-term outcome  
123 of valvular surgical procedures, there is a need to develop a computational framework which  
124 allows to generate scalable and customisable MV geometries, either 1) based on average  
125 morphometric relationships or 2) from patient-specific dimensions. A full description of the  
126 anatomy of the mitral valve has recently been made available, providing further insight into  
127 the complexity of mitral valve shape and how such information needs to be accounted for  
128 when developing geometrical models (Oliveira et al., 2020). A framework which could  
129 capture the range of morphological features required to address the high variability seen in  
130 clinical cases is not currently available and would aid in the clinical decision-making process.  
131 For example, such framework could be used to virtually evaluate mitral interventions in the  
132 case of unhealthy MV shapes by creating aimed post-repair configurations and assessing their  
133 associated biomechanics to determine the best indicators of performance.

134 The aim of this study was to develop a tool (entitled the MV toolbox) that enables the  
135 quick generation of anatomically accurate and clinically useful parametric models of the MV,  
136 which are compatible with biomechanical evaluation of mitral repair techniques through FE  
137 simulations. In this manuscript, a description of the MV toolbox is provided, including the  
138 development of the geometrical model, the equations implemented to evaluate the anatomical

139 dimensions, and the framework that generates a model ready to be used in computational  
140 modelling software.

141

## 142 **2. Mitral valve toolbox**

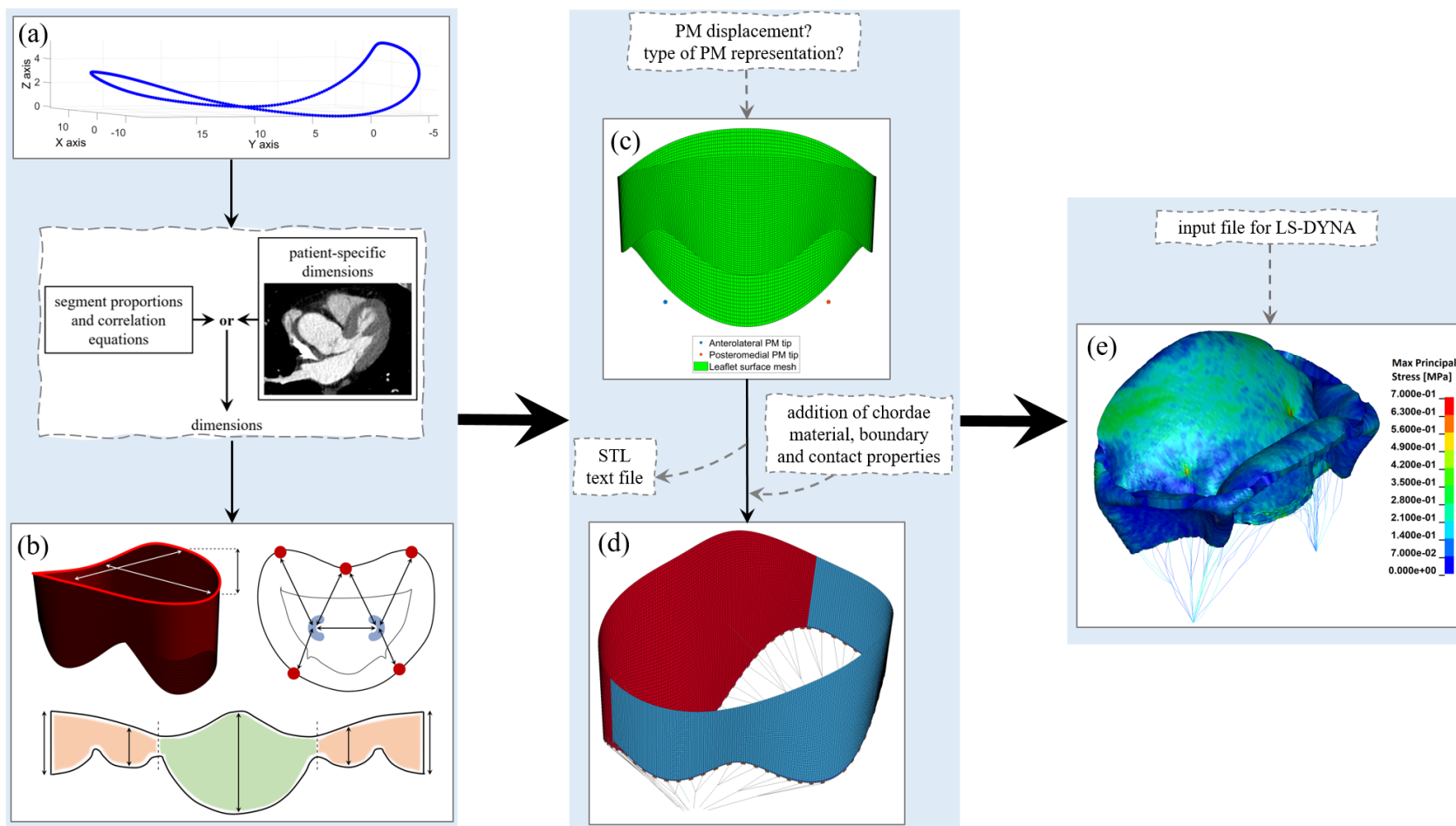
### 143 *2.1 Generic features*

144 A software toolbox that can generate the geometry of the MV as a computational  
145 model was developed and implemented in MATLAB (MATLAB<sup>®</sup>, R2019b, 9.7.0.1247435,  
146 The MathWorks Inc., Natick, MA, USA). The toolbox yields a diastolic (stress-free) MV  
147 geometry including the annulus, anterior and posterior leaflets, and a spatial representation  
148 for both PM. The model is built from a baseline mitral annular 3D profile adapted from  
149 literature (Pouch et al., 2014) and a set of key MV dimensions, used as constraints to generate  
150 the annulus and leaflet shapes. Then, PM spatial position is generated based on distances to  
151 key annular landmarks and chordae tendineae are created assuming equal spacing along the  
152 MV free edge and generated based on PM and selected free edge node coordinates.

153 The workflow of the toolbox is shown in Figure 1. The main geometric features of the  
154 MV annular and leaflet shape employed to generate the model follow mathematical  
155 proportions from recent literature (Deorsola and Bellone, 2018, Deorsola and Bellone, 2019),  
156 and PM positions and chordae tendineae distributions are based on *in vivo* and *ex vivo*  
157 findings (Yamaura, 2008, Obase et al., 2016, Lam et al., 1970). The model can be  
158 parameterized using two alternative procedures: (1) based on patient-specific dimensions  
159 obtained from patient data (e.g. medical image modalities) and directly inputted by the user  
160 or (2) using average dimensions derived from mathematical proportions relating MV  
161 anatomical segments based only on the anteroposterior (AP) diameter (Section 3).

162 Multiple graphic user interface (GUI) options are provided to better characterize the  
163 subvalvular apparatus: the user can choose a one tip point representation for the PM, where  
164 all chordae originate from, or a 3D origin scheme; moreover, PM displacement can be  
165 prescribed. Greater detail on all GUI options is provided in Section 2. The toolbox generates  
166 two different outputs: a MV geometrical model or a MV model for computational simulations  
167 (further detail on these options is presented below): Once the parameterization is completed,  
168 the MV leaflet surface mesh can be exported as a stereolithography (.stl) file, compatible with  
169 a range of modelling software (including computer-aided design and FE analysis software),  
170 and the 3D coordinates of the PM can be exported as a text file. On the other hand, if one  
171 chooses to create an input file for computational simulations, the chordae tendineae

172 distributions are also added, completing the MV model. The input file for FE simulations is  
173 compatible with LS-DYNA 4.5.12 (LSTC, Livermore CA, USA) and employs the generated  
174 geometry. For this, the meshed model is pre-processed by defining material properties,  
175 boundary conditions and contact properties through MATLAB, with the LS-DYNA input file  
176 being exported as a key (.k) file.



177

178 Figure 1. Workflow of the MV toolbox, from the generation of the morphometric model to the FE simulation result: (a) The inputs are a baseline mitral annular 3D profile  
 179 and MV dimensions, either obtained from mathematical formulations or from patient-specific medical images; (b) The model is parameterized, with the annulus, leaflets and  
 180 PM (papillary muscles) being independently scaled; (c) A surface model mesh is created for the leaflets and points identifying each PM are stored. The user can choose to  
 181 output these as an .stl file for the mesh and a text file for PM coordinates; (d) The meshed model is pre-processed: chordae tendineae are added, material properties, boundary  
 182 and contact conditions are defined; (e) The .k input file is created and run in LS-DYNA.



183 2.2 Geometrical model

184 2.2.1 Pre-processing and assumptions

185 MATLAB was used to define the annular saddle (Figure 2) based on a mean annular  
186 height to commissural width ratio (AHCWR) rotational profile for a healthy adult obtained  
187 from Pouch *et al.* (2014) which was adapted to define annular height (over the  $z$ -coordinate,  
188 displayed in Figure 2) (Pouch *et al.*, 2014). Moreover, data from Jassar *et al.* (2014) was  
189 employed to change the annulus in the  $x$ - $y$  plane (Figure 2) (Jassar *et al.*, 2014). The annulus  
190 was further reshaped to match a diastolic profile, obtaining an approximately 7.6 mm saddle-  
191 horn height, consistently with previous experimental findings (Dagum *et al.*, 2001). This  
192 annular boundary was used as a starting template from which to recreate the MV geometry  
193 (Figure 1a). The model incorporates the following assumptions, according to the GUI options  
194 chosen by the user:

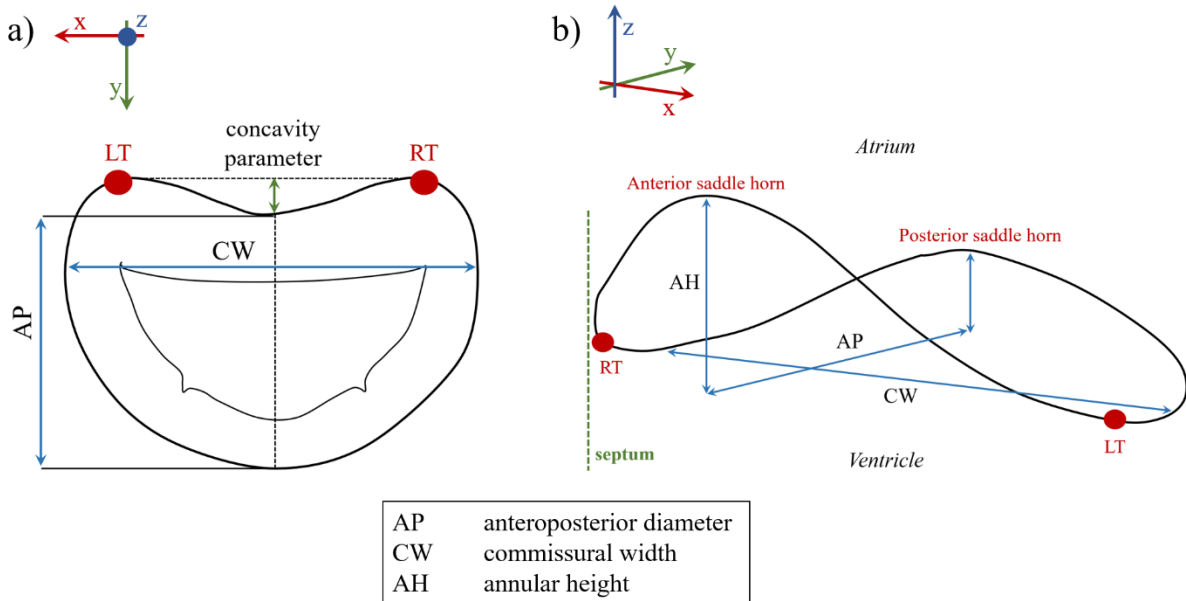
- 195 1. The annular and leaflet shapes are assumed symmetric along the long axis meridian of  
196 the anterior MV leaflet, consistent with *ex vivo* findings (Ranganathan *et al.*, 1970,  
197 Krawczyk-Ozog *et al.*, 2017) and previous geometrical models (Choi *et al.*, 2016,  
198 Stevanella *et al.*, 2009). The PM tips are assumed symmetric; however, this symmetry  
199 can be removed if asymmetric PM displacement is prescribed;
- 200 2. If an average model is selected, a healthy MV leaflet shape is reproduced, since, in  
201 disease, the proportions characterizing annular and leaflet segments change (Deorsola  
202 and Bellone, 2019). However, if patient-specific data is inputted, the model shape is  
203 not constrained when generated, and it is possible to create either a healthy or  
204 diseased MV model according to the input.

205

206

207

208



209

210 Figure 2. Input parameters requested in the toolbox to parameterize the annular boundary, where the MV  
 211 annulus is a) viewed from within the left atrium and b) from above. The 3D axis denote the orientation for each  
 212 image. Notes: LT, left trigone; RT, right trigone.

213 The generation of a morphometric MV model focuses on 3 regions: first the annulus  
 214 is parameterized, followed by the anterior and posterior leaflets, and lastly the PM tips.

215

### 216 2.2.2 Annular parameterization

217 All dimensions needed to parameterize the mitral annulus are included in Figure 2.  
 218 The valve ring has a kidney bean shape, more evident in systole, and the anterior leaflet is  
 219 centred on a slight depression in this ring (Degandt et al., 2007, Misfeld and Sievers, 2007).  
 220 Accounting for a previous mathematical study of the MV (Kaiser et al., 2019), the valve ring  
 221 concavity can be controlled given an input parameter that varies between 0 and 0.5: 0  
 222 corresponds to a D-shaped annulus, while 0.5 represents the maximum allowed concavity.

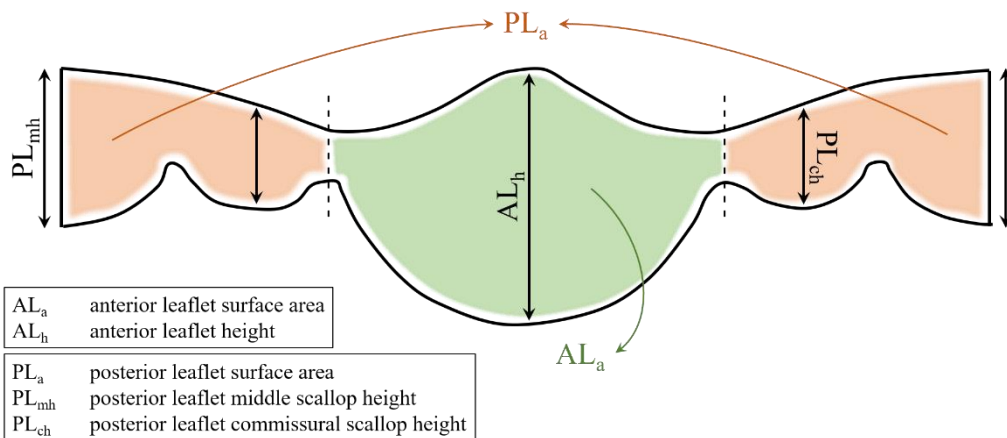
223 After defining the ring concavity, the annulus can be parameterized using three  
 224 dimensions: the AP diameter, the commissural width (CW) and the annular height (AH). The  
 225 best fitting polynomial curves were selected to manipulate the annular shape: first, they were  
 226 used to scale the AP diameter and CW in the  $x$ - $y$  plane; then, the AH was parameterized using  
 227 polynomial curves to scale  $z$  coordinates. AH was defined as the vertical distance between the  
 228 maximum and minimum annular heights (Jassar et al., 2014, Pouch et al., 2014), and, by  
 229 default, characterised as the anterior saddle horn height. By scaling this height, the posterior

230 saddle horn height was appropriately scaled, maintaining the proportion between anterior and  
 231 posterior saddle horn heights.

232

### 233 2.2.3 Leaflet parameterization

234 Given the assumed symmetry of the MV, the heights of the anterolateral and  
 235 posteromedial commissural scallops were considered equal. The required MV dimensions to  
 236 parameterize the leaflets are shown in Figure 3. The initial 3D free edge template was  
 237 generated according to the inputted leaflet heights and baseline commissural heights (to be  
 238 adapted during the implementation) reported by Ranganathan et al (Ranganathan et al.,  
 239 1970), which were interpolated.

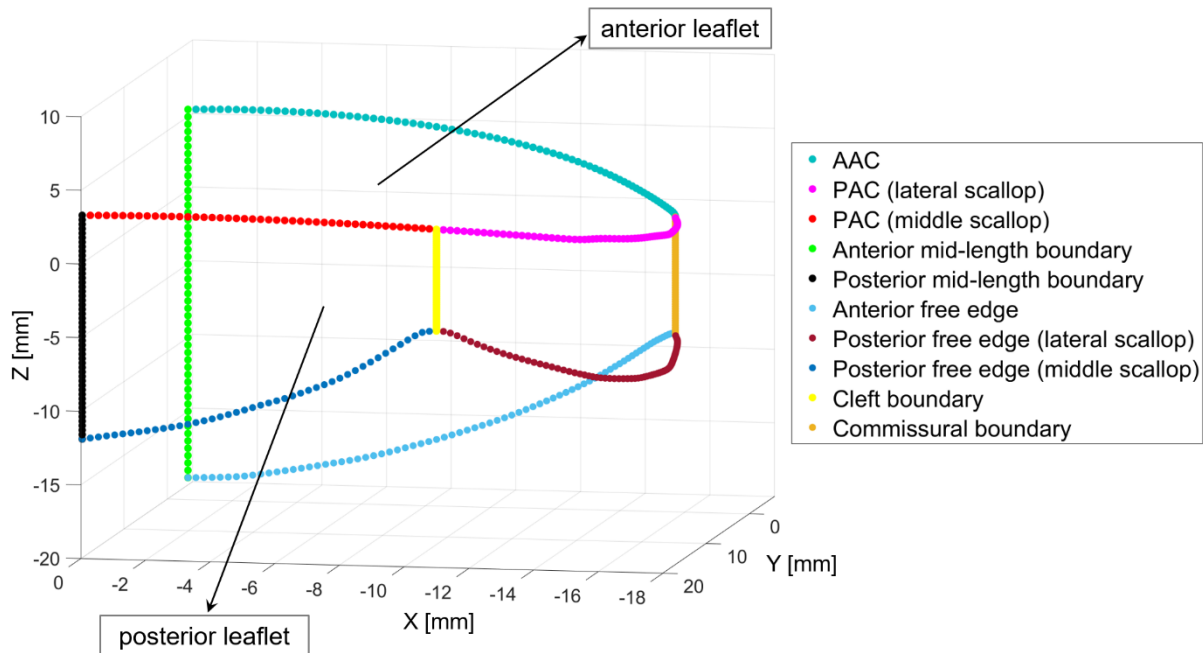


240

241 Figure 3. Input parameters requested in the toolbox to parameterize the leaflets.

242 To parameterize the leaflet surface areas, both annular and free edge boundaries were  
 243 split into different portions representing the anterior leaflet and the posterior middle and  
 244 commissural scallops. For this process, the annular boundary was first split considering  
 245 anterior and posterior annular proportions (2/5 and 3/5 of the total annular circumference,  
 246 respectively (Pouch et al., 2014, Jassar et al., 2014)). The annular split point has been set as  
 247 the commissural point. In addition, the posterior leaflet middle scallop is usually broader than  
 248 the other two scallops (Ranganathan et al., 1970, Krawczyk-Ozog et al., 2017); therefore, to  
 249 divide the posterior leaflet annular boundary between middle and commissural scallops and  
 250 in agreement with a previous morphometry study (Deorsola and Bellone, 2019), the middle  
 251 scallop was assumed equal to 9/20 of the total posterior leaflet circumference. In the  
 252 implementation, the length of the commissural and cleft boundaries was then altered to obtain

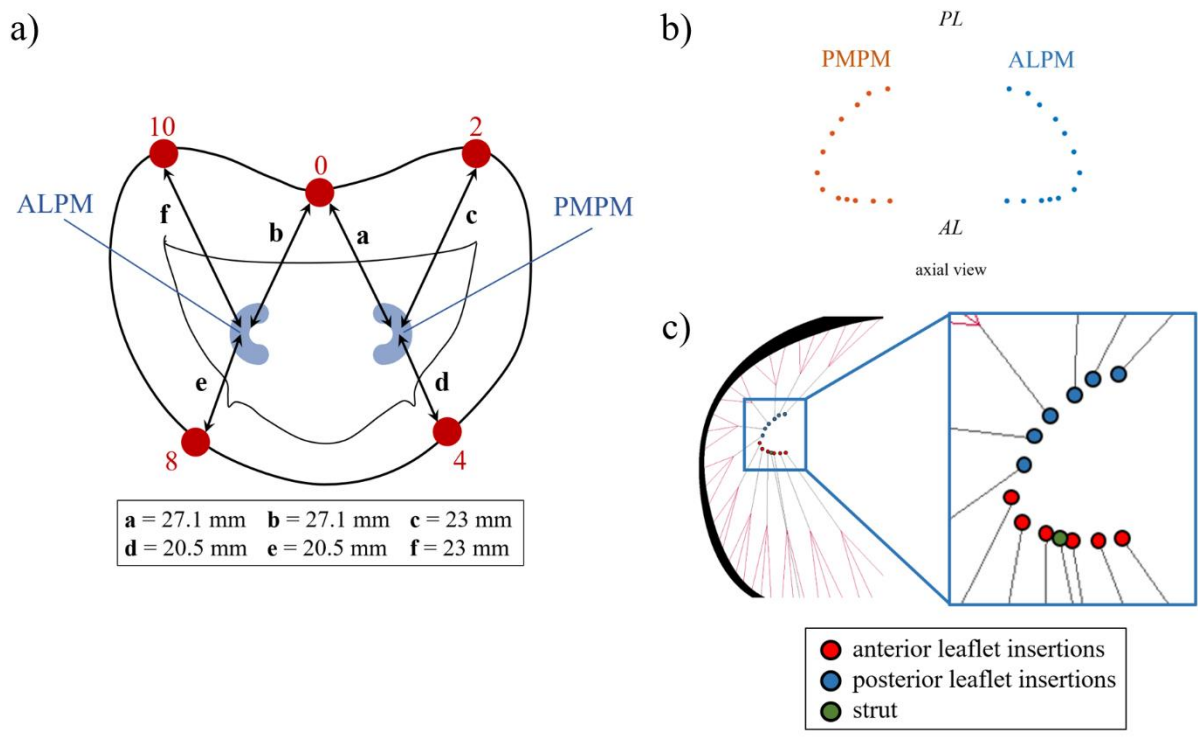
253 the desired leaflet areas. A representation of all leaflet boundaries employed is presented in  
 254 Figure 4.  
 255



256  
 257 Figure 4. The lateral half of the MV is represented, with boundaries defined during the parameterization process  
 258 of the leaflets. Notes: AAC, anterior annular circumference; PAC, posterior annular circumference.

259 **2.2.4 Papillary muscle parameterization**

260 The 3D spatial position of PM tips is parameterized according to distances between  
 261 the tips and annular landmarks (o'clock points) (Yamaura, 2008, Sakai et al., 1999). Figure  
 262 5a represents these annular points and the implemented distances (within literature ranges).  
 263 The user can decide whether to represent the PM as a single tip (where all chordae originate  
 264 from), or as a 3D point cloud of chordae origins in a C-shape (as given in an axial view),  
 265 discretized in Figure 5b and 5c and based on *in vivo* and *ex vivo* findings (Obase et al., 2016,  
 266 Lam et al., 1970) and previous computational studies (Stevanella et al., 2011, Choi et al.,  
 267 2016). This point cloud consists of 13 origin points per PM, giving rise to 12 anterior leaflet  
 268 free edge insertions, 12 posterior leaflet free edge insertions and 2 strut chordae insertions. In  
 269 total, it equals 26 chordae, consistent with *in vivo* (Obase et al., 2016) and *ex vivo* (Lam et al.,  
 270 1970) findings.



272

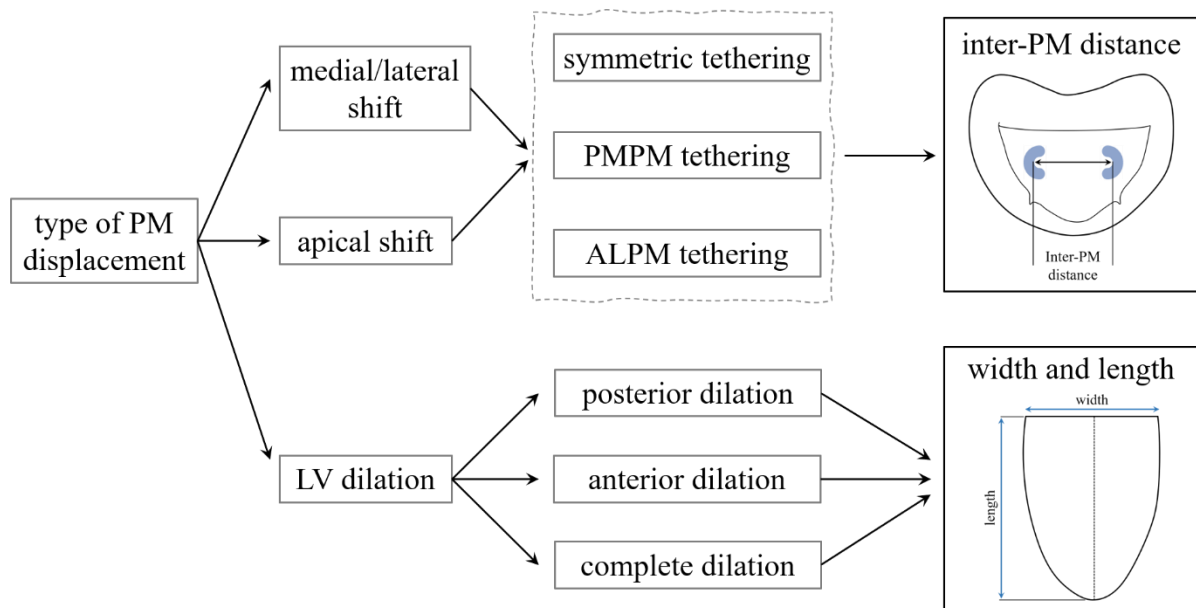
273 Figure 5. a) Distances between PM tips and corresponding points of mitral annulus, as characterized by the  
 274 literature (Sakai et al., 1999, Yamaura, 2008). 0, 2, 10, 4 and 8 o'clock represent: anterior annular midpoint;  
 275 right trigone; left trigone; division between middle and posteromedial commissural scallops; division between  
 276 middle and anterolateral commissural scallops, respectively (Yamaura, 2008); b) 3D shape representing chordae  
 277 origins in the PMs (axial view); c) Different origin points correspond to different points of insertion into the  
 278 leaflets. Notes: ALPM, anterolateral PM; PMPM, posteromedial PM; PL, posterior leaflet; AL, anterior leaflet.

279 The spatial position of PM tips can be further manipulated to represent different  
 280 dysfunctional situations (Figure 6). The PMs can undergo medial/lateral (position change in  
 281  $x$ - $y$  plane) and apical (change in the  $z$ -coordinate) shifts, corresponding to malposition or  
 282 change in position (Kim et al., 2012). These relate to symmetric (same motion restriction for  
 283 both leaflets) or asymmetric (prevalent restriction of one of the leaflets) tethering, represented  
 284 by displacement of both PMs or either one of them (Kim et al., 2012). Since these changes  
 285 are associated with altered inter-PM distances (Kim et al., 2014, Obase et al., 2016), the user  
 286 needs to provide the desired inter-PM distance as an input.

287 As the LV dilates, the PM also get displaced (Obase et al., 2016). In the toolbox, the  
 288 user can prescribe whether the LV dilates posteriorly, anteriorly, or on both sides. An .stl file  
 289 of a 18 year old (female, weight 68 kg, BSA 1.66 m<sup>2</sup>) adolescent LV model was  
 290 reconstructed from a magnetic resonance imaging (MRI) scan sequence obtained at the  
 291 Murdoch Children's Research Institute (study approved by the Human Research Ethics  
 292 Committee of the Royal Children's Hospital – HREC 33227): the left ventricle was scanned  
 293 with a cine TrueFISP short axis stack sequence, using multiple breath-hold blocks, on a

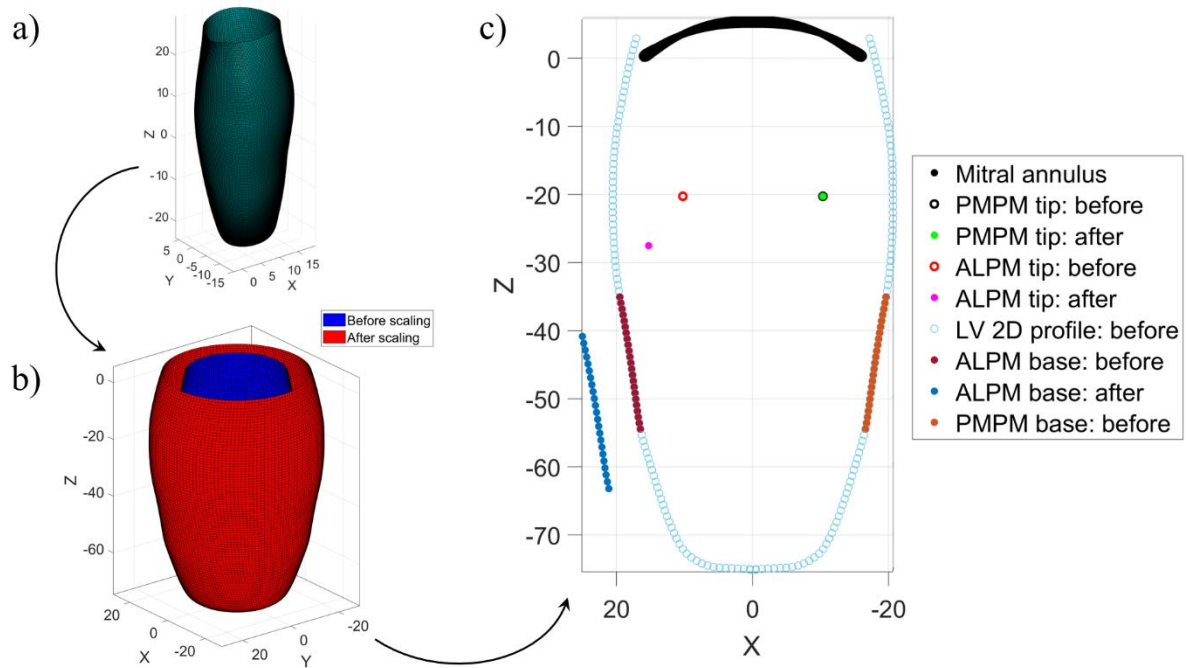
294 Siemens Aera MRI at 1.5T (repetition time = 39.6 ms; echo time = 1.43; flip angle = 80  
 295 degrees; pixel spacing  $1.33 \times 1.33$  mm; slice thickness = 7 mm; 25 frames over the cardiac  
 296 cycle).

297 The reconstructed model was used as a template to approximate the inner geometry of  
 298 the LV on which papillary muscles are placed. The model has been scaled to match adult  
 299 dimensions from the literature (Di Donato et al., 2006) and arranged in the 3D space to align  
 300 its base with the MV annular plane, similar to previous computational studies (Park et al.,  
 301 2019, Domenichini and Pedrizzetti, 2015, Domenichini et al., 2005). The geometry can be  
 302 then parameterized based on the input width and length (Park et al., 2019, Di Donato et al.,  
 303 2006, Domenichini and Pedrizzetti, 2015). The distance between the tip of each PM and its  
 304 respective site of origin at the LV wall was assumed 26 mm, yielding a PM base within the  
 305 middle third of the wall (Saha and Roy, 2018). By parameterizing the LV geometry, the  
 306 position of the PM base is also rearranged, and, if the respective distance between tip and  
 307 base is greater than 8.8 mm (standard deviation for this distance (Saha and Roy, 2018)), the  
 308 tip is displaced (as displayed in the schematic from Figure 7).



329

330 Figure 6. GUI options for the definition of PM displacement in a dysfunctional case. Notes: PM, papillary  
 331 muscle; ALPM, anterolateral papillary muscle; PMPM, posteromedial papillary muscle; LV, left ventricle.



332

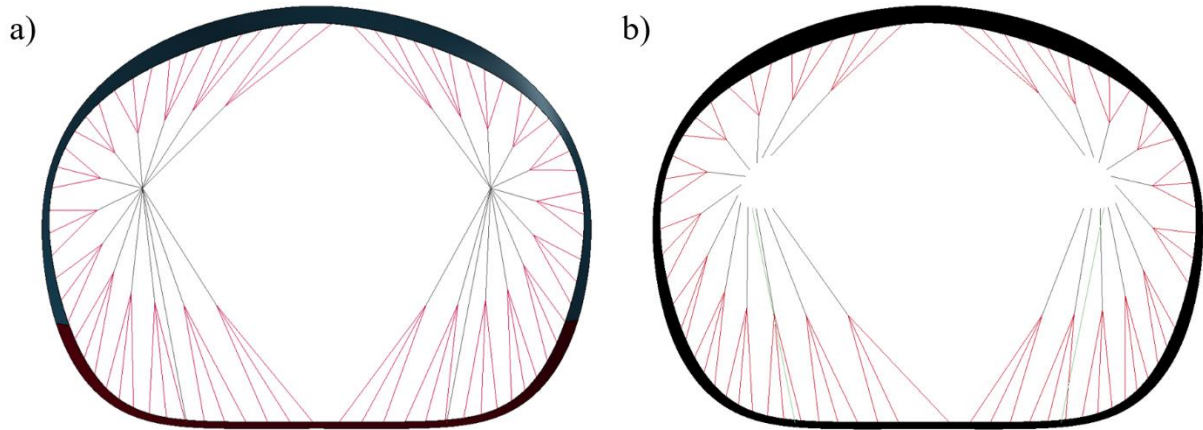
333 Figure 7. MATLAB process of PM displacement due to LV dilation: a) A LV 3D model reconstructed from  
 334 MRI imaging is employed as a template, which can be scaled according to input dimensions for width and  
 335 length (b)); c) A 2D cross-section representation of PM displacement due to LV dilation is displayed, including  
 336 positions for PMPM and ALPM before and after LV scaling. In a scenario where LV anterior dilation occurs,  
 337 the position of the anterior PM base is altered accordingly, leading to ALPM displacement. Notes: PM, papillary  
 338 muscle; ALPM, anterolateral papillary muscle; PMPM, posteromedial papillary muscle; LV, left ventricle.

339

### 340 2.2.5 Chordae generation

341 All but the strut chordae are assumed to attach at the free edge (primary chordae) and  
 342 secondary chordae are not included in the toolbox. Primary chordae are equally spaced along  
 343 the free margin and, based on the generated leaflet geometry, insertion points in the free edge  
 344 are created according to the number of chordae branches to include: they split into three  
 345 branches in the case of a single PM point and if the PM is represented with a 3D shape.  
 346 Chordae are branched at a node midway between the PM origin node and the free margin:  
 347 finding this node involves obtaining the midway point between three free margin nodes and  
 348 then the midway point between that point and the PM origin node. Examples of virtually  
 349 created chordae tendineae with a single PM tip and a 3D PM shape are shown in Figure 8.





350

351 Figure 8. a) Single PM tip (left) and b) 3D PM shape (right) chordae tendineae distributions.

352

### 353 3. Morphometric evaluation: The Golden Proportion

#### 354 3.1 Equations employed for average model

355 Recently, two clinical studies have shed light on the use of the Golden Proportion to  
 356 define the geometrical structure of the healthy MV (Deorsola and Bellone, 2018, Deorsola  
 357 and Bellone, 2019). This proportion has been observed in nature (Iosa et al., 2013, Ferring  
 358 and Pancherz, 2008, Henein et al., 2011) and consists of a ratio obtained from sectioning a  
 359 certain segment in two different parts (Deorsola and Bellone, 2018). The use of the Golden  
 360 Proportion to characterize MV geometry has been assessed by previous studies (Deorsola and  
 361 Bellone, 2018, Deorsola and Bellone, 2019) and the corresponding formulae are employed in  
 362 the MV toolbox to generate the annular and leaflet parts from one single input dimension: the  
 363 AP diameter. Further detail on this ratio can be found elsewhere (Deorsola and Bellone,  
 364 2019). The equations that define the annulus are:

$$d_{CW} = 1.236d_{AP}, \quad (1)$$

365

$$h_{AH} = 0.236d_{AP}, \quad (2)$$

366

367 where  $d_{CW}$  is the commissural width,  $h_{AH}$  is the annular height and  $d_{AP}$  is the  
 368 anteroposterior diameter. Assuming the annular boundary as a circumference, the annular  
 369 radius is equal to half of the CW. As for leaflet heights, the anterior leaflet height is defined  
 370 equal to the AP diameter and the posterior leaflet heights are defined as below:



$$P_{mh} = r = 0.618d_{AP}, \quad (3)$$

371

$$P_{ch} = 0.618^2 d_{AP}, \quad (4)$$

372

373 where  $r$  is the annular radius,  $P_{mh}$  and  $P_{ch}$  are the posterior leaflet middle and commissural  
 374 scallop heights, respectively. The leaflets are mathematically defined as half-ellipses:

$$A_a = \pi \frac{[4.236r^2]}{4} = 0.4045\pi d_{AP}^2 \quad (5)$$

375

$$P_a = \pi \frac{[2.854r^2]}{4} = 0.2725\pi d_{AP}^2 \quad (6)$$

376

377 where  $A_a$  and  $P_a$  are the anterior and posterior leaflet surface areas, respectively.

### 378 3.2 Validation

#### 379 3.2.1 Annular parameters

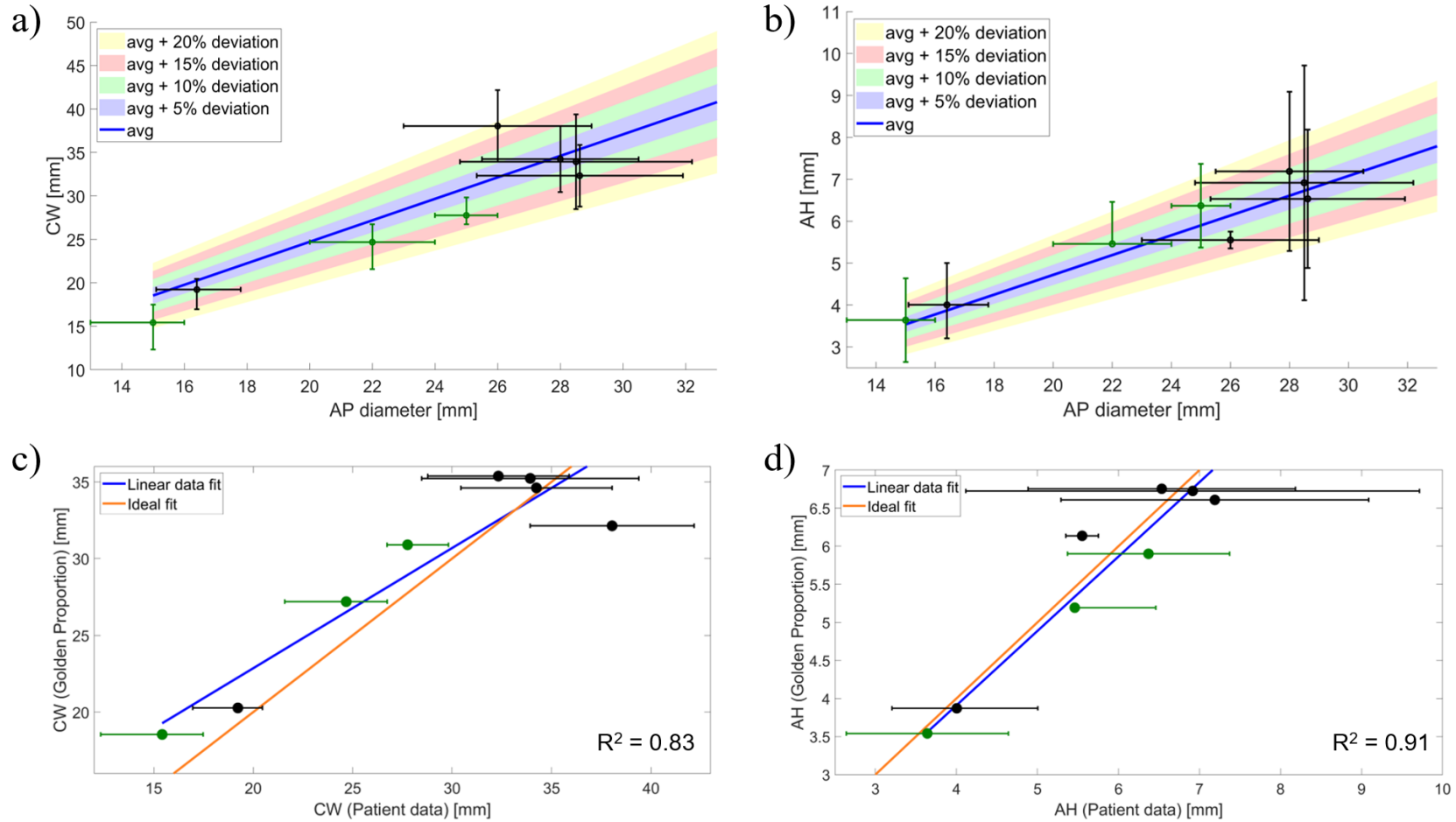
380 Given the dynamic variability in annular shape during the cardiac cycle (Jiang et al., 2014)  
 381 and the fact that the Golden Proportion equations better represent a diastolic MV  
 382 configuration (Deorsola and Bellone, 2018), mid-diastolic data was employed for validation  
 383 of the Golden Proportion predictions. For this, mid-systolic data was retrieved from adult and  
 384 paediatric *in vivo* studies and converted to mid-diastolic values: variations of -9% and +3%  
 385 were employed for AH and CW data, respectively, based on clinical findings (Tang et al.,  
 386 2019, Levack et al., 2012, Maffessanti et al., 2013). For end-systolic data, the same values  
 387 were used. Predictions for CW and AH, as provided by clinical data and derived from the  
 388 Golden Proportion, are present in Figure 9 a) and b), while goodness-of-fit is explored in  
 389 Figure 9 c) and d). The Golden Proportion equations appear able to predict CW and AH  
 390 values from the AP diameter, as given by R-squared values of 0.83 and 0.91, respectively.  
 391 The average relative errors between predicted average values and clinical ones are  $10.01 \pm$   
 392  $11.18\%$  and  $5.68 \pm 19.82\%$  for the CW and AH, respectively. While the average relative error  
 393 values are in an acceptable range, the standard deviation is greater than the respective  
 394 average. This is due to the high variability in clinical data, which can have standard  
 395 deviations as high as 13%, 16% and 37% from the average value for the AP diameter, CW

396 and AH, respectively (Mihaila et al., 2014). Despite this, the trend provided by the Golden  
397 Proportion agrees with the clinical data.

398

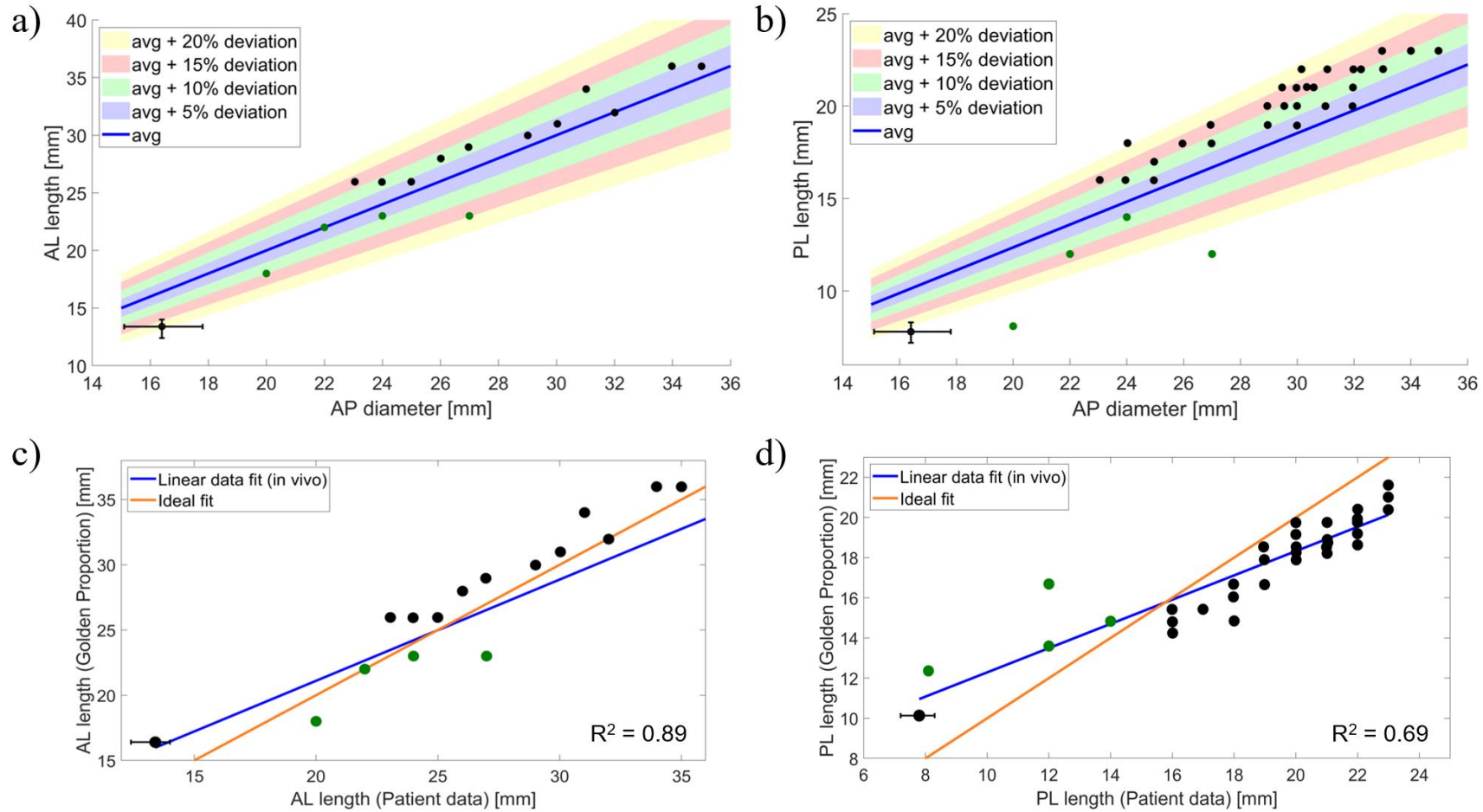
### 399 3.2.2 Leaflet lengths

400 A recent study showed good correlations between the AP diameter and leaflet lengths  
401 (both correlations with  $R^2 = 0.94$ , p-value = 0.01) (Deorsola and Bellone, 2019). Further adult  
402 and paediatric *in vivo* data was retrieved from the literature and compared with the  
403 predictions provided by the Golden Proportion, as observed in Figure 10. All adult patient  
404 data retrieved from Deorsola *et al.* (2019) (Deorsola and Bellone, 2019) is above the  
405 predicted Golden Proportion means; nonetheless, this data comes from a unique study and  
406 may have had an associated propagation error at the time of measurements, causing an  
407 overestimation of leaflet lengths from clinical images. The Golden Proportion equations do  
408 appear able to predict leaflet lengths from the AP diameter, with *in vivo* data falling within  
409 the predicted range and R-squared values being 0.89 and 0.69 for anterior (AL) and posterior  
410 (PL) leaflet lengths, respectively. Mean relative errors between predicted values and clinical  
411 measures are 7.74% and 9.01% for AL and PL lengths, respectively.



412

413 Figure 9. Predictions for commissural width (a) and annular height (b) as a function of the anteroposterior diameter, as given by the Golden Proportion (colored shades  
 414 representing up to 20% deviation from the average value) and by adult and paediatric clinical data (represented by black – adult - and dark green – paediatric - standard  
 415 deviation bars) (Pouch et al., 2014, Jassar et al., 2014, Lee et al., 2013, Mihaila et al., 2014, Jolley et al., 2017, Munin et al., 2014). A direct regression analysis is shown for  
 416 commissural width (c) and annular height (d), with the orange fitting line representing the one-to-one fit between predicted and patient data and the blue line representing the  
 417 patient data best linear fit.



418

419 Figure 10. Predictions for anterior (a) and posterior (b) leaflet lengths as a function of the anteroposterior diameter, as given by the Golden Proportion (colored shades  
 420 representing up to 20% deviation from the average value) and by adult *in vivo* data (Deorsola and Bellone, 2019, Munin et al., 2014). Black and green points represent unique  
 421 patient data for the studies from Deorsola *et al.* (2019) (Deorsola and Bellone, 2019) and Nomura *et al.* (Nomura et al., 2019), respectively. A direct regression analysis is  
 422 shown for anterior (c) and posterior (d) leaflet lengths, with the orange fitting line representing the one-to-one fit between predicted and patient data and the blue line  
 423 representing the patient data best linear fit.

424 3.2.3 Leaflet areas

425 The equations for leaflet areas, based on the Golden Proportion, yield total anterior  
 426 and posterior leaflet areas; therefore, to assess their accuracy in obtaining leaflet surface  
 427 areas, a comparison against mean total leaflet area values reported in the literature was  
 428 performed. When total leaflet area values were available, corresponding to diastole, these  
 429 were directly employed; however, most clinical studies report mean leaflet area values at  
 430 mid-systole, a time frame where the leaflets are in full coaptation, with the coapting area not  
 431 being included in the data. Therefore, to enable a comparison to be compatible between our  
 432 predictions and literature, mean diastolic leaflet areas have been estimated from mean mid-  
 433 systolic values.

434 For this estimation, the ratio between the diastolic total leaflet area and the closed  
 435 mid-systolic leaflet area (minimal area that needs to be covered by the leaflets to occlude the  
 436 mitral orifice) was employed as a scaling factor. This ratio ranges from  $1.4 \pm 0.1$  (Beaudoin  
 437 et al., 2013a, Beaudoin et al., 2013b) to  $1.63 \pm 0.17$  (Kim et al., 2019). Here, two ratios of  
 438 1.48 and 1.64 were employed to (1) obtain an estimation of the total leaflet areas from adult  
 439 and paediatric mid-systolic data reported by clinical papers and (2) assess the effect of  
 440 varying this ratio in the estimation of total leaflet area. An assessment of the average relative  
 441 errors is presented in Table 1, and predictions for AL and PL surface areas, as provided in the  
 442 literature and derived from the Golden Proportion, can be observed in Figures 9 and 10.

443

444 Table 1. Mean relative difference between Golden Proportion predictions and original mid-systolic data from  
 445 the literature, as well as estimated diastolic literature data for AL and PL areas, assuming total to closed leaflet  
 446 surface area ratios of 1.48 and 1.64.

	<i>In vivo</i> relative error [%]		
	Original literature data	Estimated diastolic data: Ratio = 1.48	Estimated diastolic data: Ratio = 1.64
AL area	84.06	$35.61 \pm 31.60$	$23.83 \pm 28.65$
PL area	73.21	$24.39 \pm 36.70$	$13.58 \pm 33.25$

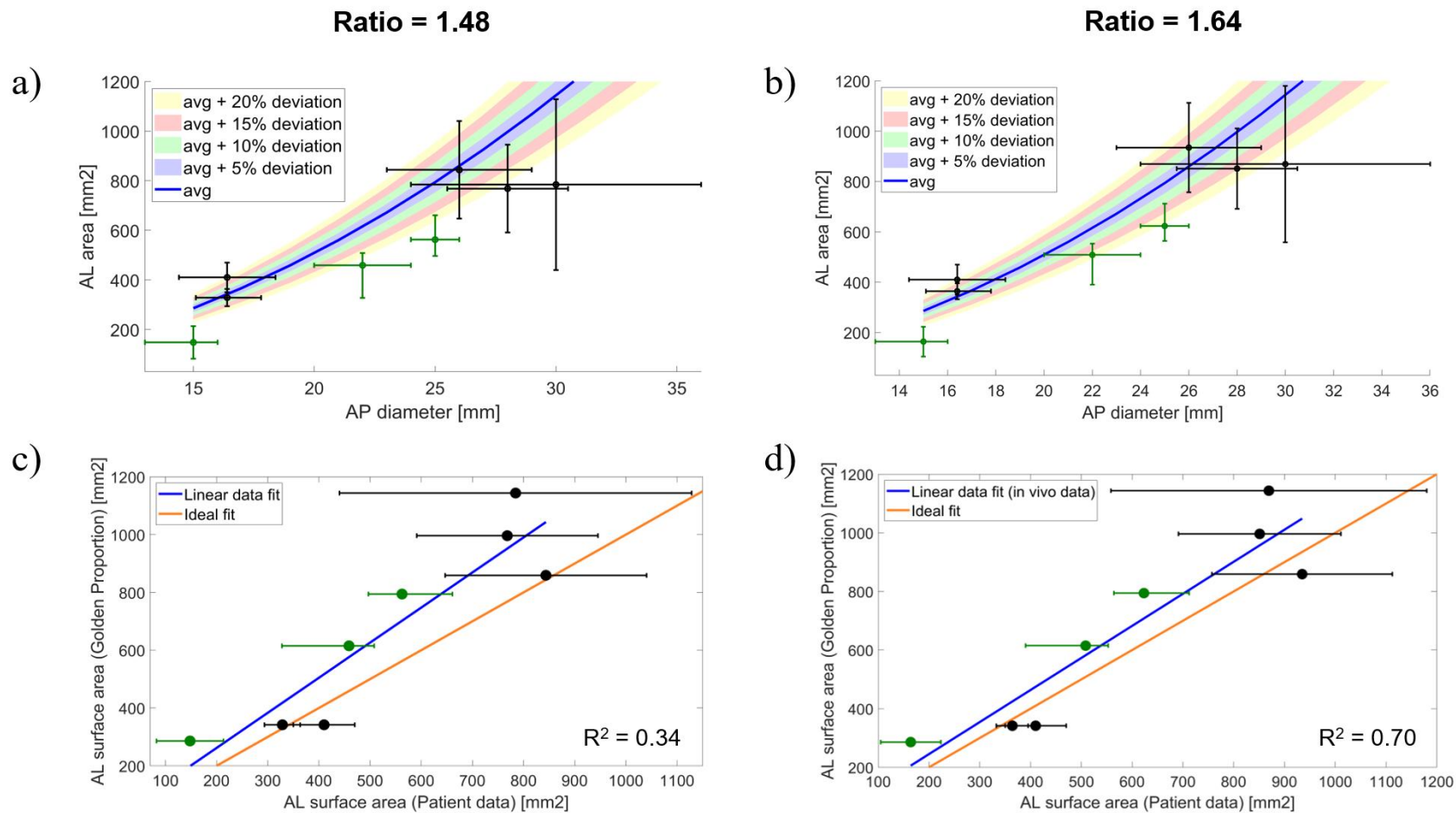
447

448 Table 1 shows that the relative difference between Golden Proportion predictions and original  
 449 mid-systolic data for leaflet areas is much greater than when comparing Golden Proportion  
 450 predictions and estimated diastolic data. This further corroborates the fact that estimating  
 451 diastolic leaflet surface areas is required to assess the validity of the Golden Proportion

452 predictions. Moreover, the relative error estimated is sensitive to the ratio used, with the  
453 average *in vivo* relative error decreasing by more than 10% for both leaflets when the ratio is  
454 increased. This ratio greatly varies amongst the AL and PL, since the literature shows ratios  
455 of  $1.32 \pm 0.39$  and  $1.47 \pm 0.50$  for AL and PL areas, respectively, for an AP diameter of  $14.3$   
456  $\pm 1.8$  mm (Debonnaire et al., 2015). In addition, the standard deviation for leaflet surface  
457 areas can be as high as 28% for the AL or 25% for the PL in a clinical sample (Mihaila,  
458 2013), which can help justify the elevated variability in literature data and in the resulting  
459 error standard deviations present in Table 1.

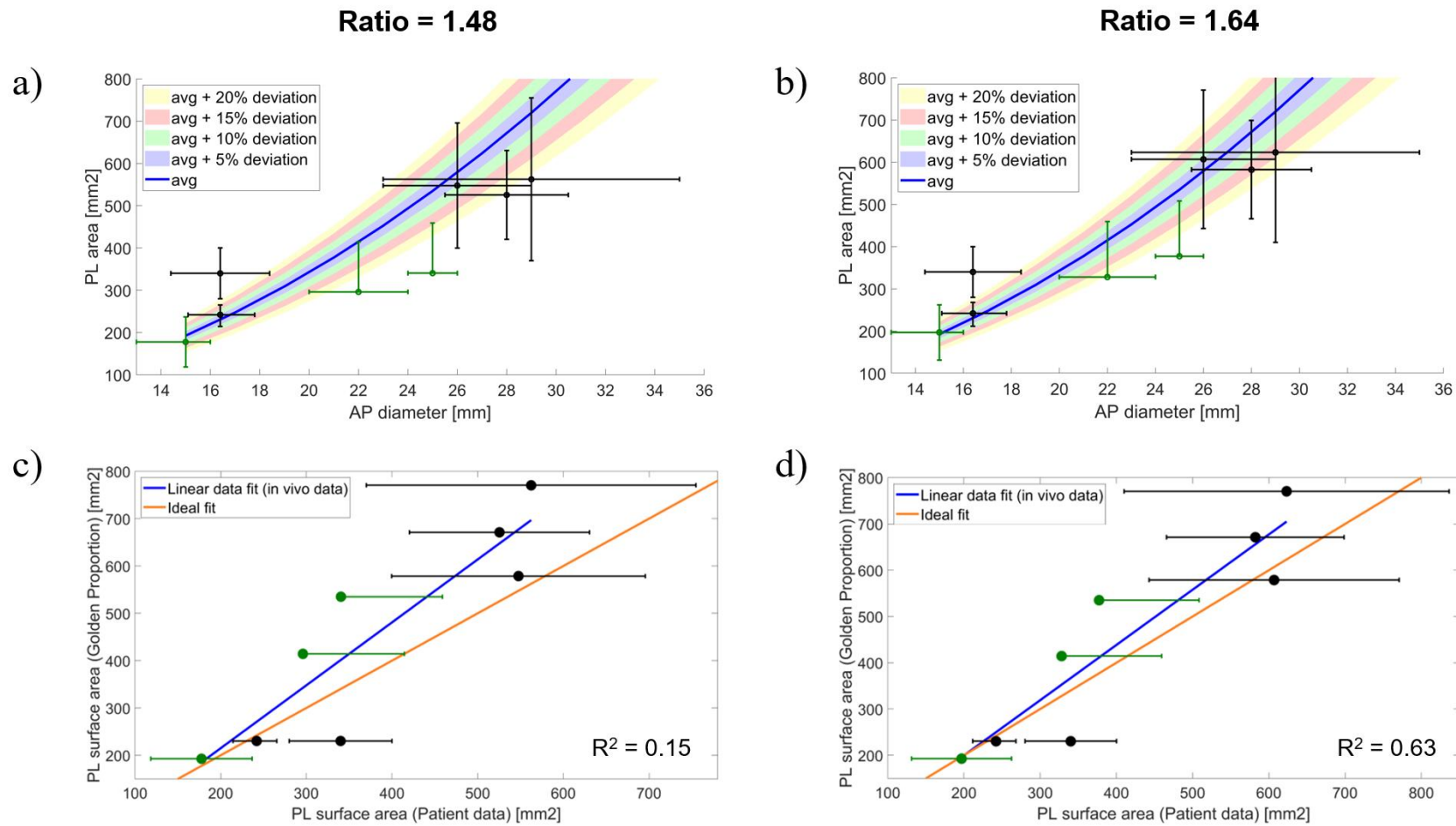
460 Figures 11 and 12 show that the *in vivo* data follows the general trend presented by the  
461 Golden Proportion predictions for leaflet surface areas, given the assumed percentage of  
462 deviation. R-squared values improve with an increasing ratio (AL: 0.34 vs 0.70; PL: 0.15 vs  
463 0.63), suggesting that the Golden Proportion better predicts leaflet surface areas with higher  
464 values.

465 Given these factors, we deemed that a 15 % range for the Golden Proportion prediction of the  
466 leaflet areas is acceptable, and, in the toolbox, a value within that range will be employed for  
467 leaflet areas.



468

469 Figure 11. Predictions for the anterior leaflet surface area as a function of the anteroposterior diameter for ratios of 1.48 (a) and 1.64 (b), as given by the Golden Proportion  
 470 (colored shades representing up to 20% deviation from the average value), by adult and paediatric clinical data (represented by black – adult - and dark green – paediatric -  
 471 standard deviation bars) (Lee et al., 2013, Mihaila, 2013, Mihaila et al., 2014, Jolley et al., 2017, Munin et al., 2014, Kim et al., 2019). A direct regression analysis is shown  
 472 for ratios of 1.48 (c) and 1.64 (d), with the orange fitting line representing the one-to-one fit between predicted and patient data and the blue line representing the patient data  
 473 best linear fit.



474

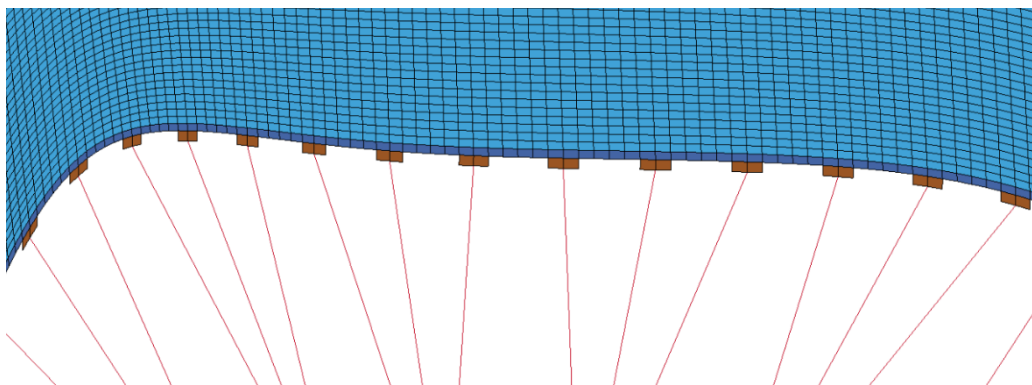
475 Figure 12. Predictions for the posterior leaflet surface area as a function of the anteroposterior diameter for ratios of 1.48 (a) and 1.64 (b), as given by the Golden Proportion  
 476 (colored shades representing up to 20% deviation from the average value), by adult and paediatric clinical data (represented by black – adult - and dark green – paediatric -  
 477 standard deviation bars) (Lee et al., 2013, Mihaila, 2013, Mihaila et al., 2014, Jolley et al., 2017, Munin et al., 2014, Kim et al., 2019). A direct regression analysis is shown  
 478 for ratios of 1.48 (c) and 1.64 (d), with the orange fitting line representing the one-to-one fit between predicted and patient data and the blue line representing the patient data  
 479 best linear fit.



480 **4. Pre-processing of the FE model**

481 The final geometrical model created by the MV toolbox corresponds to point cloud  
482 boundaries representing the annulus and the free edge. Using functions from the GIBBON  
483 toolbox (Moerman, 2018), a surface mesh is created between these boundaries: if the user  
484 wishes to export the leaflet mesh as an .stl file, triangular shell elements are chosen;  
485 alternatively, if a simulation input file is required, quadrangular shell elements are selected.  
486 Complete details on the mesh quality evaluations performed for the quadrangular mesh  
487 (ready for LS-DYNA simulations) can be found on Appendix B.

488 The pre-processing of the geometry to be used in a simulation input file is performed  
489 by adding transition elements on the leaflet free edge and creating the chordae tendineae. In  
490 LS-DYNA, chordae are discretized into beam elements (two nodes per element), combined  
491 with cable material properties, in effect transforming these elements into elastic rods which  
492 have resistance under tension, but not under compression. To better represent the movement  
493 of the chordae tendineae, each chorda branch is discretized with 6 beam elements. Moreover,  
494 two transition quadrangular shell elements are defined at each leaflet insertion point, in  
495 continuity with the leaflet free edge shell elements. These transition elements, assumed to  
496 consist of a much stiffer material than the leaflet tissue, are where chordae insert, serving to  
497 avoid local mesh warping due to the transfer of concentrated loads from chordae tendineae to  
498 leaflets (Stevanella et al., 2009). An example of the transition elements added to the model is  
499 displayed in Figure 13.



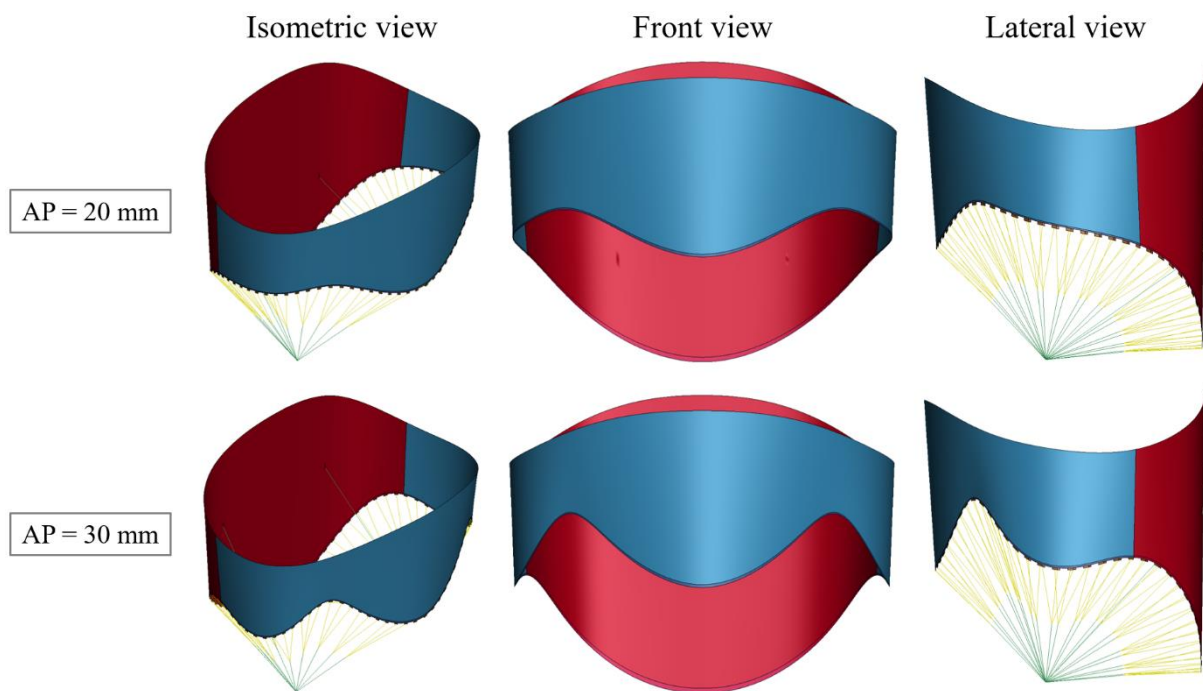
500  
501 Figure 13. Transition elements on the free margin (brown quadrangular shell elements).

502  
503  
504

505 **5. Toolbox generated models: examples**

506 A range of average and patient-specific geometries generated by the toolbox are displayed in  
507 Figures 14-18 (see Appendix C for more examples of patient-specific creations). Figure 14  
508 shows two average MV shapes obtained from different values for the AP diameter, where a  
509 greater value (30 mm) leads to greater leading dimensions governing the annulus and the  
510 leaflets when compared with a smaller value (20 mm).

511

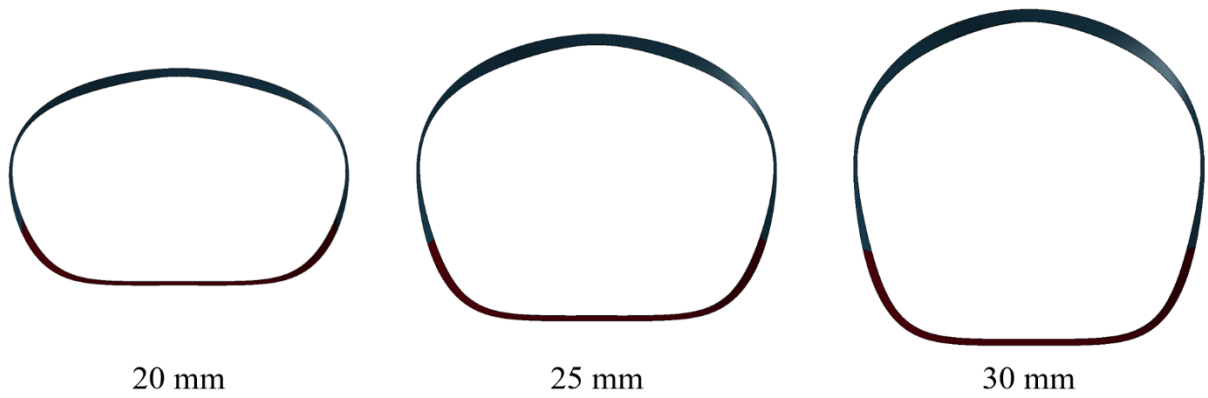


512

513 Figure 14. Average MV models generated with different AP diameters (20 and 30 mm).

514

515 Figures 15-17 show a range of geometries obtained with varying geometrical parameters  
516 individually while keeping others constant. With an increasing AP diameter, the MV annular  
517 shape tends to become more circular in shape (Figure 15). Moreover, a greater AL length leads  
518 to changes in the AL free edge profile (Figure 16) and an increased PL surface area leads to a  
519 broader PL shape (Figure 17). Apart from annular and leaflet dimensions, PM positions can  
520 also be prescribed. Figure 18 displays an example of PMPM displacement, a geometric  
521 alteration usually associated with impaired performance of the MV. Indeed, the toolbox offers  
522 flexibility to generate any desired shape: Appendix D includes LS-DYNA simulation results  
523 for average and patient-specific MV models, where the latter is a representation of a diseased  
524 valve.

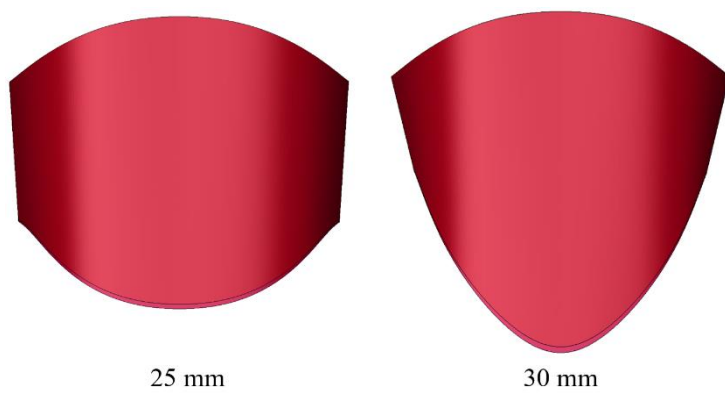


525

526

Figure 15. Mitral valve geometry obtained with the AP diameter varying between 20 and 30 mm.

527

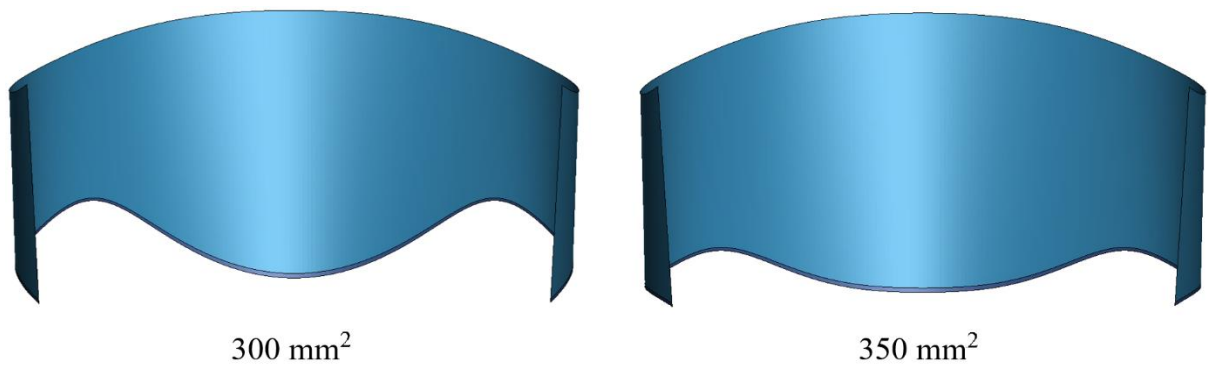


528

529

Figure 16. Mitral valve anterior leaflet geometry obtained for anterior leaflet lengths of 25 and 30 mm.

530



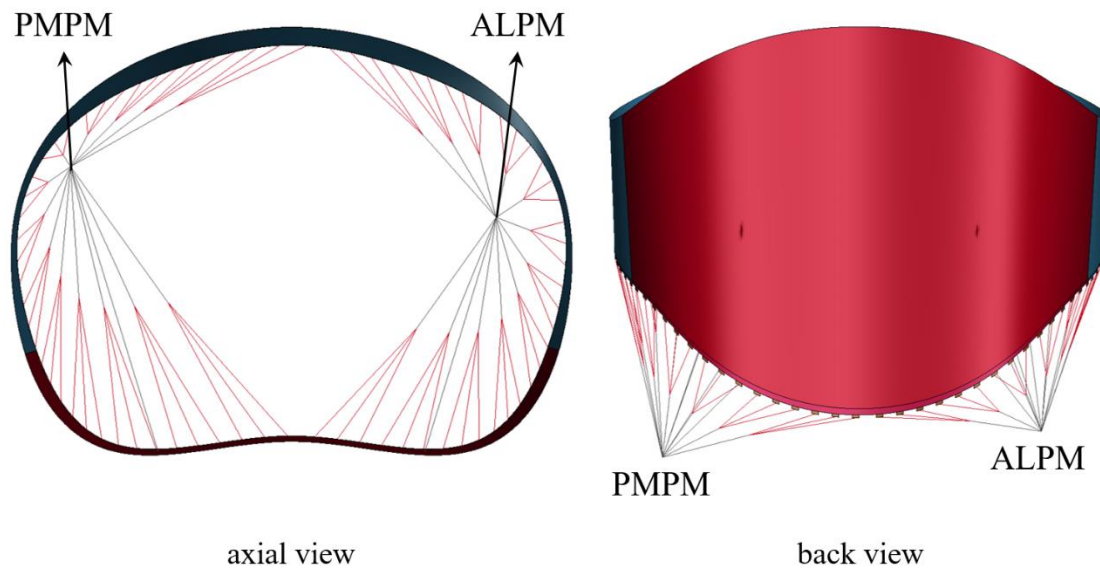
531

532

533

Figure 17. Mitral valve posterior leaflet geometry obtained for posterior leaflet areas varying between 300 and 350 mm<sup>2</sup>.

534



535

axial view

back view

536 Figure 18. Patient-specific input of PM position, with PMPM displacement represented.

537

## 538 6. Discussion

539 The MV toolbox allows for the automated and user-controlled generation of tailored  
 540 MV geometries from patient dimensions, and the creation of finite element input files for  
 541 computational biomechanical evaluation using minutes of computational time. The main  
 542 novelty behind this toolbox is that it allows to: (1) obtain a geometrical model, based on  
 543 dimensions from patient-specific imaging or on predicted values from Golden Proportion  
 544 equations; (2) create a meshed model which can be pre-processed directly in MATLAB and  
 545 (3) generate an input file for computational simulations using LS-DYNA.

546

### 547 6.1 Computational approach for the average MV model and current challenges

548 The average healthy MV shape obtained with the toolbox is based on clinical and *ex*  
 549 *vivo* data, and the models generated appear anatomically realistic, being comparable to  
 550 average (Choi et al., 2016, Alleau et al., 2019) and patient-specific (Stevanella et al., 2011,  
 551 Pham et al., 2017) models employed in other computational studies. Despite the high average  
 552 relative errors of the Golden Proportion predictions for leaflet areas against average *in vivo*  
 553 data (Section 3.2.3), very good correlations ( $R^2 = 0.94$ , p-value = 0.01) have been found  
 554 between MV leaflet lengths and the AP diameter which agreed with the Golden Proportion  
 555 (Deorsola and Bellone, 2018, Deorsola and Bellone, 2019). Moreover, all annular dimensions

556 from the literature have also shown agreement with Golden Proportion predictions (Section  
557 3.2.1).

558 In reality, MV quantitative data is associated with high variability amongst a  
559 population sample, as observed in the standard deviations from clinical data. The current  
560 limitations present in clinical imaging modalities may directly impact the derived MV  
561 morphometric data, contributing towards model uncertainty (Wu and Takeuchi, 2017). In  
562 fact, the accuracy of the measurements obtained from scans (especially leaflet areas, which  
563 need to be inferred from 3D imaging parameterizations) depend on the type of modality used,  
564 their spatial and temporal resolutions, and the operator expertise, which can introduce a bias  
565 on the obtained data. Therefore, both the variability in data and the range of accuracy of the  
566 measurements present in literature studies can help explain the elevated average relative  
567 errors obtained in this study and the standard deviation of those errors. Nonetheless, further  
568 studies are required to obtain more complete datasets of morphological measurements of the  
569 MV, which lack in the current literature. These can then be used to further validate the  
570 Golden Proportion predictions and evaluate new correlation analyses.

571 The main current challenge of the MV toolbox is the representation of the subvalvular  
572 apparatus: even though it is based on the literature (Yamaura, 2008, Sakai et al., 1999),  
573 studies describing the PM positioning in the 3D space with greater accuracy are required.  
574 Besides, current *in vivo* imaging modalities are unable to properly capture the chordae and  
575 the PM (Gao et al., 2017b), and therefore our mathematical representation and distribution of  
576 the same is based on such assumptions. This, however, does not differ from computational  
577 studies employing average mitral leaflet geometries (Choi et al., 2016, Alleau et al., 2019)  
578 and even patient-specific (Gao et al., 2017a, Biffi et al., 2019) ones, since patient-specific  
579 chordal distributions are very difficult to obtain.

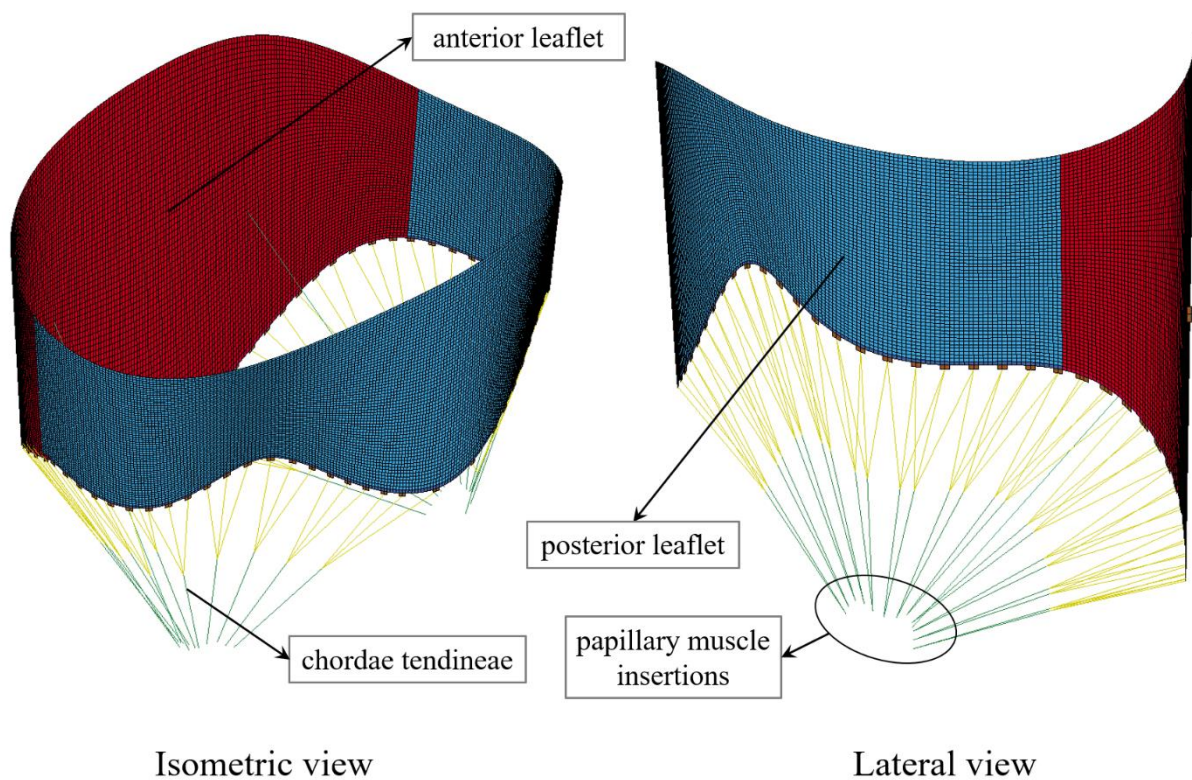
580

## 581 *6.2 Comparison with other state-of-the-art methodologies*

582 Recent studies have either 1) focused on the use of patient-specific models with  
583 valvular geometries, material properties and boundary conditions obtained from clinical data,  
584 or 2) the development of computational methodologies for the parameterization of the MV  
585 structure. While the first approach is time consuming, requiring extensive pre-processing to  
586 reconstruct the MV shape of a subject and define patient-specific modelling properties, the  
587 second approach is faster, arising as one step forward towards the clinical translation of MV  
588 models. Recent parameterization frameworks include the 2D mapping of leaflet surfaces from

589 imaging modalities for a more intuitive detection of pathology during decision making  
590 (Lichtenberg et al., 2020), the creation of 3D MV shapes from specific measurements  
591 performed in imaging modalities and their use to study the effect of transcatheter MV  
592 replacement in left ventricular outflow tract haemodynamics (Pasta et al., 2020), and a  
593 heuristic generation of chordae tendineae and PM tips (Walczak et al., 2021). While these  
594 frameworks are able to quickly generate clinically relevant MV shapes, they can only be  
595 applied to individual cases. The MV toolbox, on the other hand, is flexible, enabling the  
596 creation of morphological MV models, scalable to average human dimensions or patient-  
597 specific ones, within a timescale compatible with clinical use. In addition, the models can be  
598 directly meshed and an input file including material properties, boundary conditions and  
599 contact conditions, ready for computational simulations, can be outputted. The toolbox  
600 generates meshed models which meet criteria for numerical modelling. This means that the  
601 model pre-processing can be accelerated further, since it can be directly set up for  
602 computational simulations without other tiresome processes. As far as the authors know, our  
603 study is the first MV parametric model which allows the variation of its anatomy and has the  
604 flexibility to input the dimensions of a specific subject; subsequently generating an input file  
605 ready for numerical analysis (Figure 19).

606



607

608 Figure 19. Sample 3D MV model with all components included, ready for computational simulations.



### 609 6.3 Potential applications

610 The MV toolbox can have several end-user applications. From a clinical perspective,  
611 and given its flexibility, it can be used to study the influence of morphological MV  
612 parameters on its function. The average MV shape generated assumes a healthy valve, and  
613 degenerative valve disease, for instance, leads to significant alteration in mitral valve  
614 proportions (Deorsola and Bellone, 2019). However, inputted patient-specific parameters can  
615 be used to create a range of diseased scenarios, such as: varying annular diameters to  
616 represent different cases of annular dilation (Kim et al., 2019, Lee et al., 2013), which can  
617 compromise leaflet coaptation (Ito et al., 2017); incorporating PM displacement, which is  
618 well correlated with increased regurgitant volume in patients with functional ischemic mitral  
619 regurgitation (Obase et al., 2016, Ito et al., 2017); or increasing leaflet surface area to  
620 represent myxomatous degeneration of the MV (Clavel et al., 2015). Moreover, clinicians can  
621 use the toolbox to virtually evaluate current and novel mitral interventions, such as the use of  
622 extension biological patches to restore leaflet dimensions in the case of posterior leaflet  
623 congenital hypoplasia (Parato and Masia, 2018), or papillary muscle approximation as an  
624 adjunctive technique for MV regurgitation (Mihos et al., 2017). The toolbox can be further  
625 edited to allow for the inclusion of medical devices (such as annuloplasty rings (Kong et al.,  
626 2018)) and virtually assess their performance and influence on the biomechanics of the MV  
627 using a range of MV models through computational simulations. Ultimately, this could aid  
628 with the design optimization and customization of new devices.

629

### 630 6.4 Future work

631 This study has focused on the concept of developing a framework for the automated  
632 generation of geometrical models of the MV. This model is to be developed further,  
633 especially concerning the representation of the subvalvular apparatus: greater control on the  
634 addition process of the chordae tendineae, including the possibility of choosing different  
635 branching numbers and insertion into different portions of the leaflets, shall be implemented.  
636 Moreover, the possibilities of output for computational simulations will be extended: in  
637 addition to the already implemented ready-to-use LS-DYNA mesh, the code will be  
638 expanded to allow for output of the MV model in formats compatible with other software  
639 such as gmsh or VTK. The output for computational simulations will also be further  
640 developed: material properties will be improved by implementing a leaflet hyperelastic tissue  
641 model accounting for collagen fiber orientation. This will include using a layered shell





675 **References**

- 676 AGUILERA, H. M., URHEIM, S., SKALLERUD, B. & PROT, V. 2021. Influence of Annular  
677 Dynamics and Material Behavior in Finite Element Analysis of Barlow's Mitral Valve  
678 Disease. *Journal of Elasticity*.
- 679 AL-ATABI, M., ESPINO, D. M., HUKINS, D. W. & BUCHAN, K. G. 2012. Biomechanical  
680 assessment of surgical repair of the mitral valve. *Proc Inst Mech Eng H*, 226, 275-87.
- 681 ALLEAU, T., LANQUETIN, L. & SALSAC, A. V. 2019. Use of a parametric finite element  
682 model of the mitral valve to assess healthy and pathological valve behaviors. *Computer  
683 Methods in Biomechanics and Biomedical Engineering*, 22, S4-S5.
- 684 BEAUDOIN, J., HANDSCHUMACHER, M. D., ZENG, X., HUNG, J., MORRIS, E. L.,  
685 LEVINE, R. A. & SCHWAMMENTHAL, E. 2013a. Mitral valve enlargement in  
686 chronic aortic regurgitation as a compensatory mechanism to prevent functional mitral  
687 regurgitation in the dilated left ventricle. *J Am Coll Cardiol*, 61, 1809-16.
- 688 BEAUDOIN, J., THAI, W. E., WAI, B., HANDSCHUMACHER, M. D., LEVINE, R. A. &  
689 TRUONG, Q. A. 2013b. Assessment of mitral valve adaptation with gated cardiac  
690 computed tomography: validation with three-dimensional echocardiography and  
691 mechanistic insight to functional mitral regurgitation. *Circ Cardiovasc Imaging*, 6, 784-  
692 9.
- 693 BIAU, D. J., KERNEIS, S. & PORCHER, R. 2008. Statistics in brief: the importance of sample  
694 size in the planning and interpretation of medical research. *Clin Orthop Relat Res*, 466,  
695 2282-8.
- 696 BIFFI, B., GRITTI, M., GRASSO, A., MILANO, E. G., FONTANA, M., ALKAREEF, H.,  
697 DAVAR, J., JEETLEY, P., WHELAN, C., ANDERSON, S., LORUSSO, D.,  
698 SAUVAGE, E., MARIA BOSI, G., SCHIEVANO, S. & CAPELLI, C. 2019. A  
699 workflow for patient-specific fluid-structure interaction analysis of the mitral valve: A  
700 proof of concept on a mitral regurgitation case. *Med Eng Phys*, 74, 153-161.
- 701 CABALLERO, A., MAO, W., MCKAY, R. & SUN, W. 2020. Transapical mitral valve repair  
702 with neochordae implantation: FSI analysis of neochordae number and complexity of  
703 leaflet prolapse. *Int J Numer Method Biomed Eng*, 36, e3297.
- 704 CABALLERO, A., MAO, W. B., MCKAY, R., PRIMIANO, C., HASHIM, S. & SUN, W.  
705 2019. New insights into mitral heart valve prolapse after chordae rupture through fluid-  
706 structure interaction computational modeling (vol 8. 17306, 2018). *Scientific Reports*,  
707 9.
- 708 CHOI, A., MCPHERSON, D. D. & KIM, H. 2016. Biomechanical evaluation of the  
709 pathophysiologic developmental mechanisms of mitral valve prolapse: effect of  
710 valvular morphologic alteration. *Med Biol Eng Comput*, 54, 799-809.
- 711 CHOI, P. S., NAM, H. H., LASSO, A., HERZ, C., DROUIN, S., HARRILD, D. M.,  
712 QUARTERMAIN, M., FICHTINGER, G., MASCIO, C. E., EMANI, S. & JOLLEY,  
713 M. A. 2020. Three-Dimensional Modeling of Surgically Implanted Stent-Based Valves  
714 in the Mitral Position in Children. *Ann Thorac Surg*, 110, 670-675.
- 715 CLAVEL, M. A., MANTOVANI, F., MALOUF, J., MICHELENA, H. I., VATURY, O.,  
716 JAIN, M. S., MANKAD, S. V., SURI, R. M. & ENRIQUEZ-SARANO, M. 2015.  
717 Dynamic phenotypes of degenerative myxomatous mitral valve disease: quantitative 3-  
718 dimensional echocardiographic study. *Circ Cardiovasc Imaging*, 8.
- 719 CONG, T., GU, J., LEE, A. P., SHANG, Z., SUN, Y., SUN, Q., WEI, H., CHEN, N., SUN, S.  
720 & FU, T. 2018. Quantitative analysis of mitral valve morphology in atrial functional  
721 mitral regurgitation using real-time 3-dimensional echocardiography atrial functional  
722 mitral regurgitation. *Cardiovasc Ultrasound*, 16, 13.

723 DAGUM, P., TIMEK, T., GREEN, G. R., DAUGHTERS, G. T., LIANG, D., INGELS, N. B.,  
724 JR. & MILLER, D. C. 2001. Three-dimensional geometric comparison of partial and  
725 complete flexible mitral annuloplasty rings. *J Thorac Cardiovasc Surg*, 122, 665-73.  
726 DE OLIVEIRA, D. C. 2021. Mitral Valve Model Generator: First Release.  
727 DEBONNAIRE, P., AL AMRI, I., LEONG, D. P., JOYCE, E., KATSANOS, S.,  
728 KAMPERIDIS, V., SCHALIJ, M. J., BAX, J. J., MARSAN, N. A. & DELGADO, V.  
729 2015. Leaflet remodelling in functional mitral valve regurgitation: characteristics,  
730 determinants, and relation to regurgitation severity. *Eur Heart J Cardiovasc Imaging*,  
731 16, 290-9.  
732 DEGANDT, A. A., WEBER, P. A., SABER, H. A. & DURAN, C. M. 2007. Mitral valve basal  
733 chordae: comparative anatomy and terminology. *Ann Thorac Surg*, 84, 1250-5.  
734 DEORSOLA, L. & BELLONE, A. 2018. Coaptation Triangle and Golden Proportion in mitral  
735 valve anatomy. Does nature play with geometry? *Echocardiography*, 35, 30-38.  
736 DEORSOLA, L. & BELLONE, A. 2019. The Golden Proportion in the scallop geometry of  
737 normal mitral valves. When nature plays with jigsaw puzzles. *Echocardiography*, 36,  
738 1028-1034.  
739 DI DONATO, M., DABIC, P., CASTELVECCHIO, S., SANTAMBROGIO, C.,  
740 BRANKOVIC, J., COLLARINI, L., JOUSSEF, T., FRIGIOLA, A., BUCKBERG, G.,  
741 MENICANTI, L. & GROUP, R. 2006. Left ventricular geometry in normal and post-  
742 anterior myocardial infarction patients: sphericity index and 'new' conicity index  
743 comparisons. *Eur J Cardiothorac Surg*, 29 Suppl 1, S225-30.  
744 DOLL, N., SHEYTANOV, V., LABROUSSE, L., CHU, M. W. A., STEFANO, P.,  
745 MOKRACEK, A., BARON, O., LI, S. & GUNZINGER, R. 2019. Clinical performance  
746 of a three-dimensional saddle-shaped, rigid ring for mitral valve repair. *Eur J*  
747 *Cardiothorac Surg*, 55, 217-223.  
748 DOMENICHINI, F. & PEDRIZZETTI, G. 2015. Asymptotic Model of Fluid-Tissue  
749 Interaction for Mitral Valve Dynamics. *Cardiovasc Eng Technol*, 6, 95-104.  
750 DOMENICHINI, F., PEDRIZZETTI, G. & BACCANI, B. 2005. Three-dimensional filling  
751 flow into a model left ventricle. *J Fluid Mech*, 539, 179-198.  
752 DUPLESSIS, L. A. & MARCHAND, P. 1964. The Anatomy of the Mitral Valve and Its  
753 Associated Structures. *Thorax*, 19, 221-7.  
754 ESPINO, D. M., SHEPHERD, D. E. & BUCHAN, K. G. 2007. Effect of mitral valve geometry  
755 on valve competence. *Heart Vessels*, 22, 109-15.  
756 FERRING, V. & PANCHERZ, H. 2008. Divine proportions in the growing face. *Am J Orthod*  
757 *Dentofacial Orthop*, 134, 472-9.  
758 GAO, H., FENG, L., QI, N., BERRY, C., GRIFFITH, B. E. & LUO, X. 2017a. A coupled  
759 mitral valve-left ventricle model with fluid-structure interaction. *Med Eng Phys*, 47,  
760 128-136.  
761 GAO, H., QI, N., FENG, L., MA, X., DANTON, M., BERRY, C. & LUO, X. 2017b. Modelling  
762 mitral valvular dynamics-current trend and future directions. *Int J Numer Method*  
763 *Biomed Eng*, 33.  
764 HENEIN, M. Y., GOLDEN RATIO, C., ZHAO, Y., NICOLL, R., SUN, L., KHIR, A. W.,  
765 FRANKLIN, K. & LINDQVIST, P. 2011. The human heart: application of the golden  
766 ratio and angle. *Int J Cardiol*, 150, 239-42.  
767 HUANG, X. Y., DENG, L., ZUO, H., YANG, C., SONG, Y. H., LESPERANCE, M. & TANG,  
768 D. L. 2021. Comparisons of simulation results between passive and active fluid  
769 structure interaction models for left ventricle in hypertrophic obstructive  
770 cardiomyopathy. *Biomed Eng Online*, 20.

771 IOSA, M., FUSCO, A., MARCHETTI, F., MORONE, G., CALTAGIRONE, C., PAOLUCCI,  
772 S. & PEPPE, A. 2013. The golden ratio of gait harmony: repetitive proportions of  
773 repetitive gait phases. *Biomed Res Int*, 2013, 918642.

774 ITO, K., ABE, Y., TAKAHASHI, Y., SHIMADA, Y., FUKUMOTO, H., MATSUMURA, Y.,  
775 NARUKO, T., SHIBATA, T., YOSHIYAMA, M. & YOSHIKAWA, J. 2017.  
776 Mechanism of atrial functional mitral regurgitation in patients with atrial fibrillation: A  
777 study using three-dimensional transesophageal echocardiography. *J Cardiol*, 70, 584-  
778 590.

779 JASSAR, A. S., VERGNAT, M., JACKSON, B. M., MCGARVEY, J. R., CHEUNG, A. T.,  
780 FERRARI, G., WOO, Y. J., ACKER, M. A., GORMAN, R. C. & GORMAN, J. H.  
781 2014. Regional Annular Geometry in Patients With Mitral Regurgitation: Implications  
782 for Annuloplasty Ring Selection. *Annals of Thoracic Surgery*, 97, 64-70.

783 JIANG, L., OWAIS, K., MATYAL, R., KHABBAZ, K. R., LIU, D. C., MONTEALEGRE-  
784 GALLEGOS, M., HESS, P. E. & MAHMOOD, F. 2014. Dynamism of the mitral  
785 annulus: a spatial and temporal analysis. *J Cardiothorac Vasc Anesth*, 28, 1191-7.

786 JOLLEY, M. A., GHELANI, S. J., ADAR, A. & HARRILD, D. M. 2017. Three-Dimensional  
787 Mitral Valve Morphology and Age-Related Trends in Children and Young Adults with  
788 Structurally Normal Hearts Using Transthoracic Echocardiography. *J Am Soc*  
789 *Echocardiogr*, 30, 561-571.

790 KAISER, A. D., MCQUEEN, D. M. & PESKIN, C. S. 2019. Modeling the mitral valve. *Int J*  
791 *Numer Method Biomed Eng*, e3240.

792 KIM, D. H., HEO, R., HANDSCHUMACHER, M. D., LEE, S., CHOI, Y. S., KIM, K. R.,  
793 SHIN, Y., PARK, H. K., BISCHOFF, J., AIKAWA, E., SONG, J. M., KANG, D. H.,  
794 LEVINE, R. A. & SONG, J. K. 2019. Mitral Valve Adaptation to Isolated Annular  
795 Dilation: Insights Into the Mechanism of Atrial Functional Mitral Regurgitation. *JACC*  
796 *Cardiovasc Imaging*, 12, 665-677.

797 KIM, K., KAJI, S., AN, Y., NISHINO, T., TANI, T., KITAI, T. & FURUKAWA, Y. 2014.  
798 Interpapillary muscle distance independently affects severity of functional mitral  
799 regurgitation in patients with systolic left ventricular dysfunction. *J Thorac Cardiovasc*  
800 *Surg*, 148, 434-40 e1.

801 KIM, K., KAJI, S., AN, Y., YOSHITANI, H., TAKEUCHI, M., LEVINE, R. A., OTSUJI, Y.  
802 & FURUKAWA, Y. 2012. Mechanism of asymmetric leaflet tethering in ischemic  
803 mitral regurgitation: 3D analysis with multislice CT. *JACC Cardiovasc Imaging*, 5,  
804 230-2.

805 KOHLI, K., WEI, Z. A., SADRI, V., NETTO, T., LISKO, J. C., GREENBAUM, A. B.,  
806 BABALIAROS, V., OSHINSKI, J. N. & YOGANATHAN, A. P. 2021. A Simplified  
807 In Silico Model of Left Ventricular Outflow in Patients After Transcatheter Mitral  
808 Valve Replacement with Anterior Leaflet Laceration. *Ann Biomed Eng*, 49, 1449-1461.

809 KONG, F., CABALLERO, A., MCKAY, R. & SUN, W. 2020. Finite element analysis of  
810 MitraClip procedure on a patient-specific model with functional mitral regurgitation. *J*  
811 *Biomech*, 104, 109730.

812 KONG, F., PHAM, T., MARTIN, C., ELEFTERIADES, J., MCKAY, R., PRIMIANO, C. &  
813 SUN, W. 2018. Finite element analysis of annuloplasty and papillary muscle relocation  
814 on a patient-specific mitral regurgitation model. *PLoS One*, 13, e0198331.

815 KRAWCZYK-OZOG, A., HOLDA, M. K., SORYSZ, D., KOZIEJ, M., SIUDAK, Z.,  
816 DUDEK, D. & KLIMEK-PIOTROWSKA, W. 2017. Morphologic variability of the  
817 mitral valve leaflets. *J Thorac Cardiovasc Surg*, 154, 1927-1935.

818 LAM, J. H., RANGANATHAN, N., WIGLE, E. D. & SILVER, M. D. 1970. Morphology of  
819 the human mitral valve. I. Chordae tendineae: a new classification. *Circulation*, 41,  
820 449-58.

821 LEE, A. P., HSIUNG, M. C., SALGO, I. S., FANG, F., XIE, J. M., ZHANG, Y. C., LIN, Q.  
822 S., LOOI, J. L., WAN, S., WONG, R. H., UNDERWOOD, M. J., SUN, J. P., YIN, W.  
823 H., WEI, J., TSAI, S. K. & YU, C. M. 2013. Quantitative analysis of mitral valve  
824 morphology in mitral valve prolapse with real-time 3-dimensional echocardiography:  
825 importance of annular saddle shape in the pathogenesis of mitral regurgitation.  
826 *Circulation*, 127, 832-41.

827 LEVACK, M. M., JASSAR, A. S., SHANG, E. K., VERGNAT, M., WOO, Y. J., ACKER, M.  
828 A., JACKSON, B. M., GORMAN, J. H., 3RD & GORMAN, R. C. 2012. Three-  
829 dimensional echocardiographic analysis of mitral annular dynamics: implication for  
830 annuloplasty selection. *Circulation*, 126, S183-8.

831 LICHTENBERG, N., EULZER, P., ROMANO, G., BRCIC, A., KARCK, M., LAWONN, K.,  
832 DE SIMONE, R. & ENGELHARDT, S. 2020. Mitral valve flattening and parameter  
833 mapping for patient-specific valve diagnosis. *Int J Comput Assist Radiol Surg*, 15, 617-  
834 627.

835 MAFFESENTI, F., GRIPARI, P., PONTONE, G., ANDREINI, D., BERTELLA, E.,  
836 MUSHTAQ, S., TAMBORINI, G., FUSINI, L., PEPI, M. & CAIANI, E. G. 2013.  
837 Three-dimensional dynamic assessment of tricuspid and mitral annuli using  
838 cardiovascular magnetic resonance. *Eur Heart J Cardiovasc Imaging*, 14, 986-95.

839 MIHAILA, S., MURARU, D., PIASENTINI, E., MIGLIORANZA, M. H., PELUSO, D.,  
840 CUCCHINI, U., ILICETO, S., VINERANU, D. & BADANO, L. P. 2014.  
841 Quantitative analysis of mitral annular geometry and function in healthy volunteers  
842 using transthoracic three-dimensional echocardiography. *J Am Soc Echocardiogr*, 27,  
843 846-57.

844 MIHAILA, S., MURARU, D., CASABLANA, S., PELUSO, D., CUCCHINI, U., DEL  
845 BIANCO, L., VINERANU, D., ILICETO, S., BADANO, L. 2013. Three-dimensional  
846 changes in mitral valve annulus geometry in organic and functional mitral regurgitation:  
847 insights for mitral valve repair. *Eur. Heart J.*, 34, 4751.

848 MIHOS, C. G., YUCEL, E. & SANTANA, O. 2017. The role of papillary muscle  
849 approximation in mitral valve repair for the treatment of secondary mitral regurgitation.  
850 *Eur J Cardiothorac Surg*, 51, 1023-1030.

851 MISFELD, M. & SIEVERS, H. H. 2007. Heart valve macro- and microstructure. *Philos Trans*  
852 *R Soc Lond B Biol Sci*, 362, 1421-36.

853 MOERMAN, K. M. 2018. GIBBON: The Geometry and Image-Based Bioengineering add-  
854 On. *JOSS*, 3, 506.

855 MUNIN, M. A., THIERER, J., RAGGIO, I. M., GOERNER, M. S., LOMBARDERO, M.,  
856 GODIA, J., SÁNCHEZ, G. A., SPERNANZONI, F., ORTEGA, J. & TORRES, V.  
857 2014. Three Dimensional Echocardiographic Analysis of Mitral Valve Characteristics.  
858 *Rev Argent Cardiol*, 82, 279-284.

859 NCHO, B. E., PIERCE, E. L., BLOODWORTH, C. H. T., IMAI, A., OKAMOTO, K., SAITO,  
860 Y., GORMAN, R. C., GORMAN, J. H., 3RD & YOGANATHAN, A. P. 2020.  
861 Optimized mitral annuloplasty ring design reduces loading in the posterior annulus. *J*  
862 *Thorac Cardiovasc Surg*, 159, 1766-1774 e2.

863 NOMURA, K., AJIRO, Y., NAKANO, S., MATSUSHIMA, M., YAMAGUCHI, Y.,  
864 HATAKEYAMA, N., OHATA, M., SAKUMA, M., NONAKA, T., HARI, M.,  
865 UTSUMI, M., SAKAMOTO, K., IWANE, K. & KUNINAKA, N. 2019.  
866 Characteristics of mitral valve leaflet length in patients with pectus excavatum: A single  
867 center cross-sectional study. *PLoS One*, 14, e0212165.

868 OBASE, K., WEINERT, L., HOLLATZ, A., FAROOQUI, F., ROBERTS, J. D., MINHAJ, M.  
869 M., TUNG, A., CHANEY, M., OTA, T., JEEVANANDAM, V., YOSHIDA, K., MOR-  
870 AVI, V. & LANG, R. M. 2016. Elongation of chordae tendineae as an adaptive process

871 to reduce mitral regurgitation in functional mitral regurgitation. *Eur Heart J Cardiovasc*  
872 *Imaging*, 17, 500-9.

873 OKAMOTO, H., ITOH, Y. & NARA, Y. 2007. Geometric analysis of the anterior mitral leaflet  
874 and mitral valve orifice in cadaveric hearts. *Circ J*, 71, 1794-9.

875 OLIVEIRA, D., SRINIVASAN, J., ESPINO, D., BUCHAN, K., DAWSON, D. &  
876 SHEPHERD, D. 2020. Geometric description for the anatomy of the mitral valve: A  
877 review. *J Anat*, 237, 209-224.

878 PARATO, V. M. & MASIA, S. L. 2018. Hypoplasia or Absence of Posterior Leaflet: A Rare  
879 Congenital Anomaly of The Mitral Valve in Adulthood - Case Series. *J Cardiovasc*  
880 *Echogr*, 28, 45-47.

881 PARK, J., GEIRSSON, A. & BONDE, P. N. 2019. Mathematical Blueprint of a Mitral Valve.  
882 *Semin Thorac Cardiovasc Surg*.

883 PASTA, S., CANNATA, S., GENTILE, G., AGNESE, V., PILATO, M. & GANDOLFO, C.  
884 2020. Simulation of left ventricular outflow tract (LVOT) obstruction in transcatheter  
885 mitral valve-in-ring replacement. *Med Eng Phys*, 82, 40-48.

886 PHAM, T., KONG, F., MARTIN, C., WANG, Q., PRIMIANO, C., MCKAY, R.,  
887 ELEFTERIADES, J. & SUN, W. 2017. Finite Element Analysis of Patient-Specific  
888 Mitral Valve with Mitral Regurgitation. *Cardiovasc Eng Technol*, 8, 3-16.

889 POUCH, A. M., VERGNAT, M., MCGARVEY, J. R., FERRARI, G., JACKSON, B. M.,  
890 SEHGAL, C. M., YUSHKEVICH, P. A., GORMAN, R. C. & GORMAN, J. H. 2014.  
891 Statistical Assessment of Normal Mitral Annular Geometry Using Automated Three-  
892 Dimensional Echocardiographic Analysis. *Annals of Thoracic Surgery*, 97, 71-77.

893 RANGANATHAN, N., LAM, J. H., WIGLE, E. D. & SILVER, M. D. 1970. Morphology of  
894 the human mitral valve. II. The valve leaflets. *Circulation*, 41, 459-67.

895 SAHA, A. & ROY, S. 2018. Papillary muscles of left ventricle-Morphological variations and  
896 it's clinical relevance. *Indian Heart J*, 70, 894-900.

897 SAKAI, T., OKITA, Y., UEDA, Y., TAHATA, T., OGINO, H., MATSUYAMA, K. & MIKI,  
898 S. 1999. Distance between mitral anulus and papillary muscles: anatomic study in  
899 normal human hearts. *J Thorac Cardiovasc Surg*, 118, 636-41.

900 SALGO, I. S., GORMAN, J. H., 3RD, GORMAN, R. C., JACKSON, B. M., BOWEN, F. W.,  
901 PLAPPERT, T., ST JOHN SUTTON, M. G. & EDMUNDS, L. H., JR. 2002. Effect of  
902 annular shape on leaflet curvature in reducing mitral leaflet stress. *Circulation*, 106,  
903 711-7.

904 SHEN, X., WANG, T., CAO, X. & CAI, L. 2017. The geometric model of the human mitral  
905 valve. *PLoS One*, 12, e0183362.

906 STEVANELLA, M., MAFFESSANTI, F., CONTI, C. A., VOTTA, E., ARNOLDI, A.,  
907 LOMBARDI, M., PARODI, O., CAIANI, E. G. & REDAELLI, A. 2011. Mitral Valve  
908 Patient-Specific Finite Element Modeling from Cardiac MRI: Application to an  
909 Annuloplasty Procedure. *Cardiovascular Engineering and Technology*, 2, 66-76.

910 STEVANELLA, M., VOTTA, E. & REDAELLI, A. 2009. Mitral valve finite element  
911 modeling: implications of tissues' nonlinear response and annular motion. *J Biomech*  
912 *Eng*, 131, 121010.

913 SUN, X., JIANG, Y., HUANG, G., HUANG, J., SHI, M., PANG, L. & WANG, Y. 2019.  
914 Three-dimensional mitral valve structure in predicting moderate ischemic mitral  
915 regurgitation improvement after coronary artery bypass grafting. *J Thorac Cardiovasc*  
916 *Surg*, 157, 1795-1803 e2.

917 TANG, Z., FAN, Y. T., WANG, Y., JIN, C. N., KWOK, K. W. & LEE, A. P. 2019. Mitral  
918 Annular and Left Ventricular Dynamics in Atrial Functional Mitral Regurgitation: A  
919 Three-Dimensional and Speckle-Tracking Echocardiographic Study. *J Am Soc*  
920 *Echocardiogr*, 32, 503-513.

- 921 WALCZAK, L., TAUTZ, L., NEUGEBAUER, M., GEORGII, J., WAMALA, I.,  
922 SUNDERMANN, S., FALK, V. & HENNEMUTH, A. 2021. Interactive editing of  
923 virtual chordae tendineae for the simulation of the mitral valve in a decision support  
924 system. *Int J Comput Assist Radiol Surg*, 16, 125-132.
- 925 WARRAICH, H. J., CHAUDARY, B., MASLOW, A., PANZICA, P. J., PUGSLEY, J. &  
926 MAHMOOD, F. 2012. Mitral annular nonplanarity: correlation between annular  
927 height/commissural width ratio and the nonplanarity angle. *J Cardiothorac Vasc*  
928 *Anesth*, 26, 186-90.
- 929 WENK, J. F., RATCLIFFE, M. B. & GUCCIONE, J. M. 2012. Finite element modeling of  
930 mitral leaflet tissue using a layered shell approximation. *Med Biol Eng Comput*, 50,  
931 1071-1079.
- 932 WENK, J. F., ZHANG, Z., CHENG, G., MALHOTRA, D., ACEVEDO-BOLTON, G.,  
933 BURGER, M., SUZUKI, T., SALONER, D. A., WALLACE, A. W., GUCCIONE, J.  
934 M. & RATCLIFFE, M. B. 2010. First finite element model of the left ventricle with  
935 mitral valve: insights into ischemic mitral regurgitation. *Ann Thorac Surg*, 89, 1546-  
936 53.
- 937 WU, V. C. & TAKEUCHI, M. 2017. Three-Dimensional Echocardiography: Current Status  
938 and Real-Life Applications. *Acta Cardiol Sin*, 33, 107-118.
- 939 XU, F., JOHNSON, E. L., WANG, C., JAFARI, A., YANG, C., SACKS, M. S.,  
940 KRISHNAMURTHY, A. & HSU, M. 2021. Computational investigation of left  
941 ventricular hemodynamics following bioprosthetic aortic and mitral valve replacement.  
942 *Mech Res Commun*, 112.
- 943 YAMAURA, Y., ET AL. 2008. Three-Dimensional Echocardiographic Measurements of  
944 Distance Between Papillary Muscles and Mitral Annulus: Assessment With Three-  
945 Dimensional Quantification Software System. *J Echocardiogr*, 6, 67-73.
- 946 ZHANG, L. W., ADEMILOYE, A. S. & LIEW, K. M. 2019. Meshfree and Particle Methods  
947 in Biomechanics: Prospects and Challenges. *Archives of Computational Methods in*  
948 *Engineering*, 26, 1547-1576.

949